UNIVERSITI PUTRA MALAYSIA

SYNTHESIZING AND CHARACTERIZING OF YBCO SUPERCONDUCTOR VIA THERMAL TREATMENT METHOD AT DIFFERENT SINTERING TEMPERATURE

NUR AFIQAH BINTI MOHAMED INDERA ALIM SAH

SYNTHESIZING AND CHARACTERIZING OF YBCO SUPERCONDUCTOR VIA THERMAL TREATMENT METHOD AT DIFFERENT SINTERING TEMPERATURE

by

NUR AFIQAH BINTI MOHAMED INDERA ALIM SAH

(197955)

Thesis Submitted to the Department of Physics, Faculty of Science, University Putra Malaysia, in partial fulfillment of the Requirements for the Degree of Bachelor of Science in Physics with Education (Honours)
January 2022

DEDICATION

To My Father & Mother:

Mohamed Indera Alim Sah Bin Jamaludin & Norma Binti Ismail

My Beloved Siblings:

Nor Athirah

Mohd Iqbal

Nur Ainaa

Nuha

ABSTRACT

SYNTHESISING AND CHARACTERISING OF YBCO SUPERCONDUCTOR VIA THERMAL TREATMENT METHOD AT DIFFERENT SINTERING TEMPERATURE

By

NUR AFIQAH BINTI MOHAMED INDERA ALIM SAH

197955

FEBRUARY 2022

Supervisor: Mohd Mustafa Awang Kechik (PhD)

Faculty: Faculty of Science

Among the active and extensively distributed elements in physics that are receiving attention all around the globe is a superconductor. It offers zero resistance to electrical current, repelling magnetic fields, and holds enormous potential for the future. Thus, this research seeks to synthesize a high purity Y-123 superconducting system by using the thermal treatment method and comparing the effect of different sintering temperatures on the superconducting properties of Y-123. In the meantime, it also explores the study of the physical properties in microstructure, phase formation and critical temperature, T_c of Y-123. In this research, $YBa_2Cu_3O_{7-\delta}$ (Y-123) sinter at temperatures of 920 ℃, 950 ℃ and 980 ℃.

The microstructure and superconducting properties of Y-123 were investigated by thermogravimetric analyzer (TGA), X-ray diffraction (XRD), field-emission scanning electron microscope (FESEM), energy dispersive X-ray diffraction (EDX) alternating current susceptibility (ACS) and Four Point Probe (4PP). It was observed the sample Y-123 showed that the primary phases in all the XRD patterns were the orthorhombic crystal structure while Y-211 and $BaCuO_2$ act as secondary phases. The sample Y-123 with sintering temperature 980 ℃ revealed the highest value of $T_{c\text{-onset}}$, T_{cj}, T_p and the sharpest diamagnetic transition in the normalized susceptibility curves. According to the microstructure analysis, the sample with the highest average grain size is 1.285 μm was sintered at 980 ℃. On the other hand, from 4PP analysis, the sample of sintering temperature 980 ℃ exhibits good metallic behavior in the normal state with the increasing value of $T_{c\text{-onset}}$, $T_{c\text{-offset}}$, hole concentration and smallest ΔT for Y-123.

ABSTRAK

MENSINTESIS DAN MENCIRIKAN SUPERKONDUKTOR YBCO MELALUI KAEDAH RAWATAN TERMA PADA SUHU PENSINTERAAN YANG BERBEZA

Oleh

NUR AFIQAH BINTI MOHAMED INDERA ALIM SAH

197955

FEBRUARI 2022

Penyelia: Mohd Mustafa Awang Kechik (PhD)
Fakulti: Fakulti Sains

Antara unsur aktif dan secara meluas dalam fizik yang mendapat perhatian di seluruh dunia ialah superkonduktor. Ia menawarkan rintangan sifar kepada arus elektrik, menolak medan magnet, dan mempunyai potensi yang besar untuk masa hadapan. Oleh itu, penyelidikan ini bertujuan untuk mensintesis sistem superkonduktor Y-123 ketulenan tinggi dengan menggunakan kaedah rawatan haba dan membandingkan kesan suhu pensinteran yang

berbeza ke atas sifat superkonduktor Y-123. Dalam pada itu, ia juga meneroka kajian sifat fizikal dalam mikrostruktur, pembentukan fasa dan suhu kritikal, T_c Y-123. Dalam penyelidikan ini, $YBa_2Cu_3O_{7-\delta}$ (Y-123) ialah superkonduktor suhu tinggi yang mensintesis melalui rawatan haba dengan suhu pensinteran berbeza 920 ℃, 950 ℃ dan 980 ℃. Struktur mikro dan sifat superkonduktor Y-123 telah disiasat oleh analisis penganalisis termogravimetrik (TGA), pembelauan sinar-X (XRD), mikroskop elektron pengimbasan pancaran medan (FESEM), pembelauan sinar-X penyebaran tenaga (EDX) kepekaan arus ulang-alik (ACS) dan Kuar Empat Mata (4PP). Sampel Y-123 menunjukkan bahawa fasa utama dalam semua corak XRD adalah struktur hablur ortorombik manakala Y-211 dan $BaCuO_2$ bertindak sebagai fasa sekunder. Sampel Y-123 dengan suhu pensinteran 980 ℃ mendedahkan nilai tertinggi $T_{c\text{-onset}}$, T_{cj}, T_p dan peralihan diamagnet paling tajam dalam lengkung kerentanan ternormal. Menurut analisis struktur mikro, sampel dengan saiz butiran purata tertinggi ialah 1.285 μm telah disinter pada 980 °C. Sebaliknya, daripada analisis 4PP, sampel suhu pensinteran 980 ℃ mempamerkan tingkah laku logam yang baik dalam keadaan normal dengan peningkatan nilai $T_{c\text{-onset}}$, $T_{c\text{-offset}}$, kepekatan lubang dan ΔT terkecil untuk Y-123.

ACKNOWLEDGEMENTS

First and foremost, I would like to extent my deepest praise to Allah s.w.t that has given strength, determination and courages to complete this project. I would like to express my utmost gratitude to my supervisor, Assoc. Prof. Dr. Mohd Mustafa Awang Kechik for constant monitoring, guidance, valuable advice, suggestion and constructive critics during this period of study. Without constant encouragement and support from Dr, this project would not have been possible to accomplish.

Special thanks to the all the laboratory assistents, Ms. Norhaslinda Noruddin, Ms. Kamsiah Alias and Mrs. Irmazian Abd Shukor who have been helping and guide me with their technical expertise.

Next, I would like to dedicate my thankfulness to all Post graduate students, especially Mrs. Yap Siew Hong for the patience, time, endless guidance and always been there with me throughout this project. I'll remember the most famous words that you always uttered to me, " always pray for a good result." for my entire life.

A scholarship from Lembaga Zakat Negeri Kedah are gratefully acknowledge.

I would like to express my fullest appreciation to my parents and siblings, En. Indera (Abah), Pn. Norma (Mak), Kak Athirah, Abang Syamir, Iqbal, Ainaa, Nuha and Hayyan for their prayer and do'a.

Finally, I would like to thanks the special person who always supports me in his prayer. I am also grateful for being able to met this five girls, Farzana, Darwishah, Alyani, Aisyah, Illya and Faizatul for being such a special part of my degree journey, Thank you.

TABLE OF CONTENTS

LIST OF FIGURES

LIST OF TABLE

LIST OF ABBREVIATIONS

Å	Angstrom
ACS	AC-Susceptometer
BCS	Bardeen Cooper Schrieffer
EDX	Energy Dispersive X-ray
δ	Oxygen Content
g	Gram
HTS	High Temperature Superconductor
K	Kelvin
KHz	Kilohertz
λ	Wavelength
MAGLEV	Magnetic Levitation
Min	Minute
MRI	Magnetic Resonance Imaginary
℃	Degree Celsius
SEM	Scanning Electron Microscope
θ	Angle
T_c	Critical Temperature
$T_{c\text{-onset}}$	Onset Critical Temperature
$T_{c\text{-offset}}$	Offset Critical Temperature
ΔT	Critical Temperature Range
×	Magnification
XRD	X-ray Diffraction
YBCO	Yttrium Barium Copper Oxide

Y-123	$YBa_2Cu_3O_{(7-\delta)}$

Chapter 1

INTRODUCTION

1.1 Introduction of Superconductor

In this era, we need to discover and develop something new to help us in the future to struggle with the deficiency of fossil fuel per year, a massive challenge of climate change, and untangle this difficulty we can utilize by using renewable energy. Renewable energy is energy that we found from natural sources, including sunlight and wind, which it is never-ending and constantly replenished. As everyone knows, energy and sustainability are two of humanity's significant challenges. Therefore, we should preserve energy and enhance energy efficiency in the electrical system. Hence, renewable energy technologies would be able to contribute their maximum capabilities to energy security, tackling climate change, and economic growth (Kaygusuz, 2012).

In the face of rapid population growth and economic expansion, the demand for electrical energy is growing dramatically. Therefore, the electrical system that we used nowadays is exceptionally efficient, especially when transporting electricity between one

source to another. However, our electrical energy still needed further research and improvement to find a better conductor that has better efficiency, cheapest and is environmental-friendly. Rising in energy efficiency will curtail the need to invest in energy supplies.

Hence, superconductors played a significant role in our electrical system. The term "superconductor" usually refers to a material capable of supervising the electricity without zero resistance which has no energy loss while in the superconducting state. Generally, at room temperature in some materials such as metallic or compound elements, it offers a low quantity of resistance and it is known as its critical temperature. Once a critical temperature is reached, electrons are transferred regularly from one atom to another atom by using a particular material, thus, the material is called superconductive material.

The discovery of the world of superconductivity was founded in 1911 by Heike Kamerlingh Onnes, Dutch Physicist of Leiden University when he experimented with materials absolute zero temperature (Bharat, 2018). By reason of his contribution of materials at low temperature in 1913, he got a Nobel prize in Physics. Onnes found that below 4.2 K, the immeasurable value will reach due to the electrical resistance mercury is dropping (Ali, 2015) In 1973, a few alloys were discovered, such as niobium, germanium, and super conductive at a high temperature of 23 K (Bharat, 2018).

1.2 Properties of Superconductors

Superconducting materials have shown some remarkable properties that are vital for modern technology. The study on these properties is currently ongoing to identify and utilize these features in various fields. Hence, the two most essential basic properties in a superconductor are Zero Electrical Resistance and Meissner Effect.

1.2.1 Zero Electrical Resistance

In the superconducting phase, the material of the superconductor exhibits zero electrical resistance when the material cooled below its transition temperature until the resistance will become abruptly fall to zero. For example, mercury shows zero resistance under 4.2 K where it can be seen in Figure 1.1. In addition, below 4.2 K, Onnes discovered that the current continues to flow without any heat dissipation. There is no energy loss along the material since the material's resistance has been lowered to zero. Moreover, a superconducting state is existing when the state of matter in which resistance is zero (Owens & Poole, 1992).

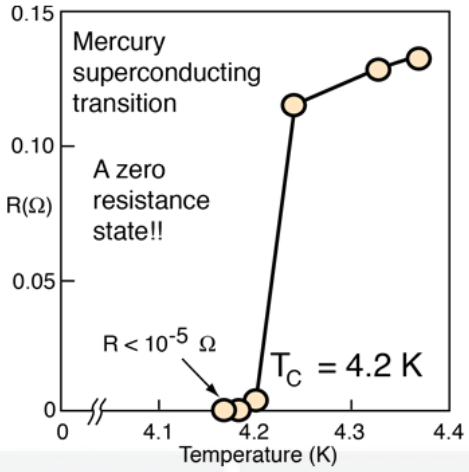

Figure 1.1: The temperature curve of mercury resistance reveals its decrease when it becomes superconducting. This was the first observation of superconductivity made by Kamerlingh Onnes in 1911 (Owens & Poole, 1992).

1.2.2 Meissner Effect

The second characteristic property of the superconducting state which known as Meissner effect, took 22 more years to be discovered. This property was explored by the German professor Alexander Meissner and his graduate student R. Ochsenfeld in 1933. This phenomenon occurs when a material transitions from the normal to superconducting state and expels all the magnetic field from within itself. A superconductor has no noticeable effect when a magnetic field is applied above the critical temperature, T_c since the magnetic field can cross through the superconductor without any barriers (Bardeen, 1955). However, if the superconductor is below its critical temperature T_c, the magnetic field will be expelled from the interior and bent around, as seen in Figure 1.2.

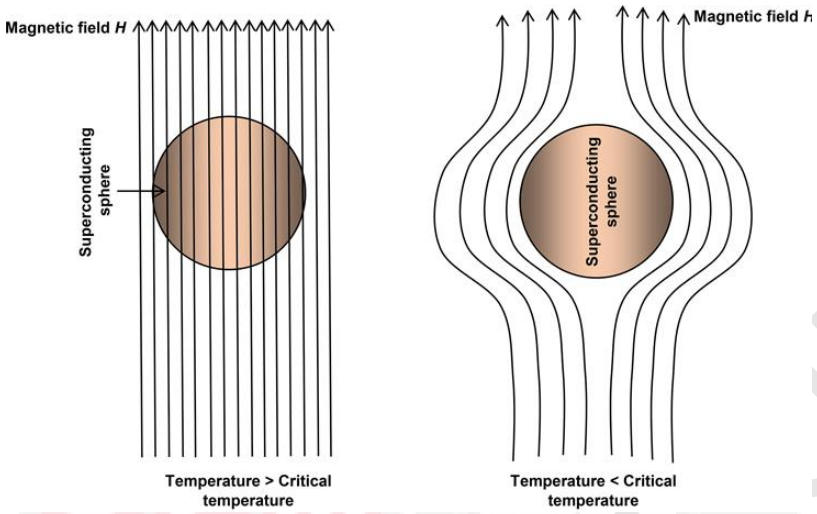

(a) **(b)**

Figure 1.2: A comparison on how a superconductor behaves when it is above and below its critical temperature, T_c. (a) The magnetic field is permitted to pass through the superconductor when it is above the critical temperature. (b) The magnetic field lines will bend around the superconductor if it is below the critical temperature (Khanna, 2017).

1.3 Application of Superconductors

The peculiar properties of superconductivity facilitated many significant discoveries of the twentieth century. Superconductors manage to execute tasks more economically with unique properties than normal conductors in this modern world. The advancement in superconductors could assist the nation in various fields, including medical, transportation, and others.

1.3.1 Magnetic Resonance Imaging (MRI)

In medicine, high-tech equipment is provided to diagnose the problem at hand. Thus, Magnetic Resonance Imaging (MRI) is one example of high-tech technology that practiced superconductivity. As a result, these devices can provide stronger fields, have more temporal stability, and have higher field uniformity than their permanent and resistive magnet equivalents (Tadic & Fallone, 2012). The procedure for examining the soft parts of the body by using Magnetic Resonance Imaging (MRI) required a person to be placed in a large and uniform electromagnet with high magnetic field. Hence, superconducting magnet played an essential role to generate high magnetic field and due to zero resistance of superconductors, the current will flow without heating the material, allowing a very high field value of 3.0 T for routine clinical care and 7.0 T for pre-clinical research (Aarnink & Overweg, 2012). Figure 1.3 showed the modern MRI that consisting a superconductors magnet inside it. In contrast, Figure 1.4 showing the x, y, and z gradients may be utilised in combination to create image slices in any direction, which is one of MRI's greatest strengths as a diagnostic tool.

Nowadays, Magnetic Resonance Imaging (MRI) was prominent and utilized the most due to the novel coronavirus diseases (COVID-19) pandemic has spread with shocking rapidity across the world. This disease tends to attack the respiratory system until it becomes severely damaged (Vasilev et al., 2021). Most of the cases are reported that there are findings related to COVID-19 pneumonia where all these cases underwent MRI from head to chest (Fields et al., 2021). Therefore, three studies were carried out to compare MRI and computerized tomography (CT) whether these instruments can reveal characteristic features of COVID-19 pneumonia (Fields et al., 2021). Overall, the results indicate that MRI satisfactorily differentiates between different phases of parenchymal infiltration compared to chest CT (Fields et al., 2021). Although CT is preferable to MRI in diagnosing pneumonia in

immunocompromised patients, MRI is an essential imaging tool that may be utilized, especially in the follow-up of these patients (Ekinci et al., 2017).

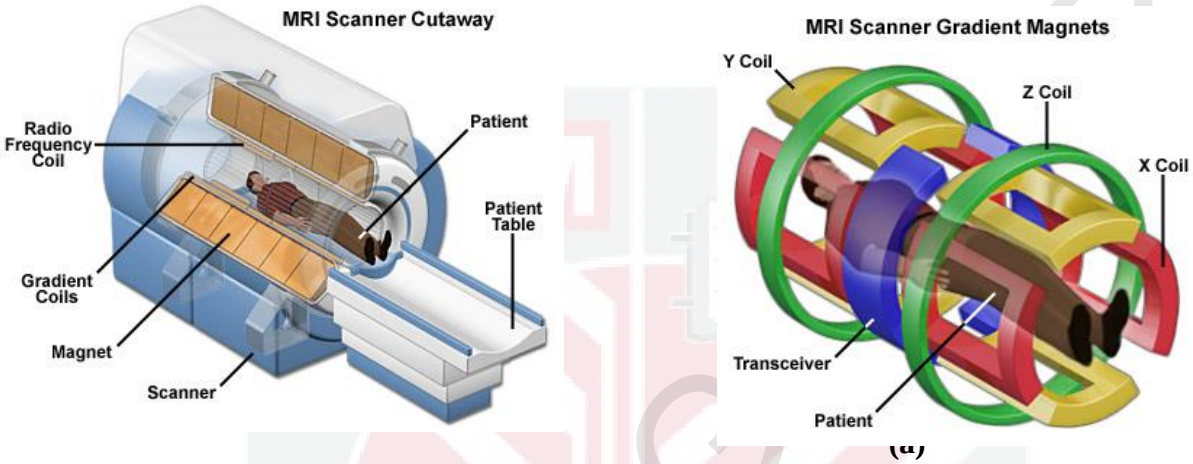

Figure 1.3: (a) MRI Scanner Cutaway (b) MRI Scanner Gradient Magnets (Resources from MRI: A Guided Tour,2015).

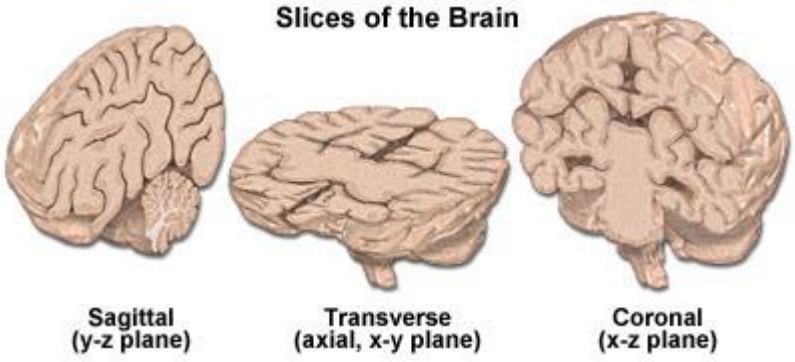

Figure 1.4: The slices of the brain in any direction (Resources from MRI: A Guided Tour, 2015).

1.3.2 Magnetic Levitation (Maglev) Train

In the transportation world, the Magnetic levitation train, known as Maglev train, is a floating vehicle that used superconducting magnets by magnetic attraction or repulsion. Using superconducting magnets in Maglev, it will assist the trains and help in reducing friction by replacing wheels with electromagnets and levitates on the guideway, generating propulsion electromechanically without any interaction (H. W. Lee et al., 2006). In contrast, a conventional train uses friction between wheels and rails to propel itself forward (H. W. Lee et al., 2006). The image of the wheel-on-rail system and Maglev is shown in Figure 1.5. Besides, Maglev used a common knowledge in physics principle applying magnetic forces concept to perform their task. Therefore, the Maglev train is the finest choice to satisfy all the requirements needed in transportation. Figure 1.6 showed a maglev train component that contributes to creating the maglev train remarkably advantageous nowadays.

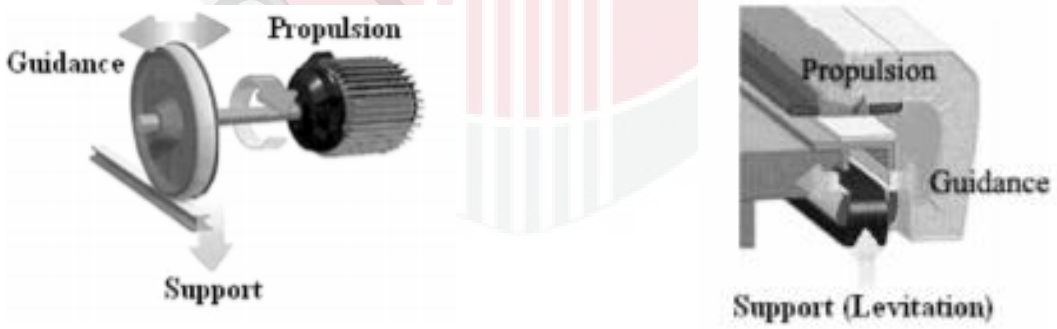

(a) **(b)**

Figure 1.5: The figure of wheel-on-rail system and Maglev (a) wheel-on-rail. (b) Maglev (H. W. Lee et al., 2006).

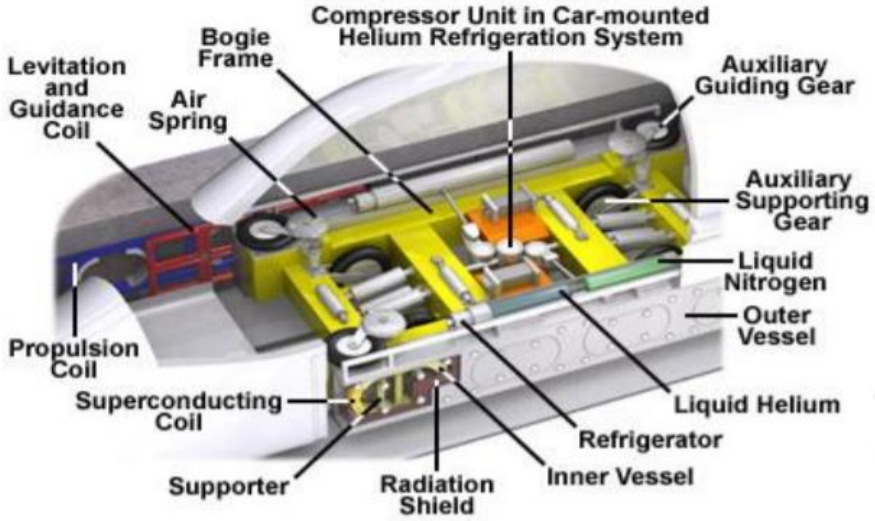

Figure 1.6: The internal component of Maglev trains (Divekar & Ekbote, 2019).

1.4 Problem Statement of This Research

The problem statements of this research:

1. The preparation method used is an essential step in producing high-quality Y-123 powder. A few different kinds of preparation methods such as thermal treatment method, solid state method, and co-precipitate. The method that used in the research will affect the physical properties of the YBCO system.

2. Several YBCO suitable for high sintering temperature due to superconductors being very delicate towards the changes of sintering temperature where it will affect superconductivity properties.

1.5 Objective of This Research

The objective for of this research project is:

1. To synthesis a good quality Y-123 superconducting system using the thermal treatment method.

2. To compare the effect of different sintering temperatures on superconducting properties of Y-123 and to study the physical properties in microstructure, phase formation and critical temperature T_c of Y-123.

Chapter 2

THEORY AND LITERATURE REVIEW

This chapter will discuss details about the phenomenological of superconductivity and literature study. This chapter will also explain about YBCO system and the effect of heat treatment on YBCO.

2.1 The Phenomenon of Superconductivity

As mentioned before in chapter 1, Heike Kamerlingh Onnes discovered the phenomena of superconductivity in 1911. He is a Dutch physicist who spent the rest of his life working and doing research at Leiden University. This phenomenon of superconductivity is one of the most common in today's world, and it is one of the most essential branches of condensed matter physics (Wolf, 1992). A phenomenon known as superconductivity exists at very low temperature, and each superconductor has its own transition temperature, T_c. Below transition temperatures, T_c it will remain as superconductors, and superconductors above transition temperatures T_c will behave as normal metal (Owens & Poole, 1992).

On 10 July 1908, Heike Kamerlingh Onnes was in his laboratory at Leiden University when he had a remarkable moment during his work experience when he first liquefied helium

which occur at 4.2 Kelvin and this research lead him to introduce a brand-new chapter in physics about low-temperature (Van Delft & Kes, 2010). On that day, he achieved a value as low as 1 Kelvin of temperature (Van Delft & Kes, 2010). This liquefying process happened when helium gas is compressed to a lower amount, causing the temperature to increase. The compressed gas would then become warmer and it will flow through a pipe enclosed by a more excellent fluid. The cooler fluid can help in the absorption of heat from the gas and transfer it to the fluid (Owens & Poole, 1992). Next, the cooler gas that is still compressed is pushed into a small hole where it will expand and the cooling phase will occur. The process will be repeated many times until it liquefies where the temperature of compressed gas achieves 4.2 K. Onnes' method of liquifying helium is still utilised in modern refrigerators (Owens & Poole, 1992).

2.2 Classification of Superconductor

Superconductors are classified into two types which are Type-I and Type-II (Babaev & Speight, 2005) as can be seen in Figure 2.1. These two types of superconductors are observed based on their behaviour against magnetic field penetration (Owens & Poole, 1992). In addition, Figure 2.2 showed the elements in the periodic table that can undergo a superconducting state.

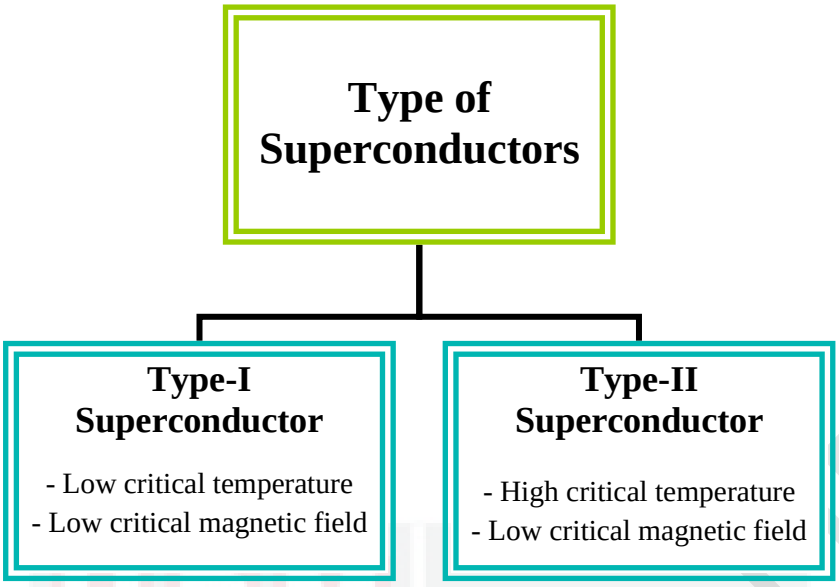

Figure 2.1: Types-I and II compare their behaviour and properties.

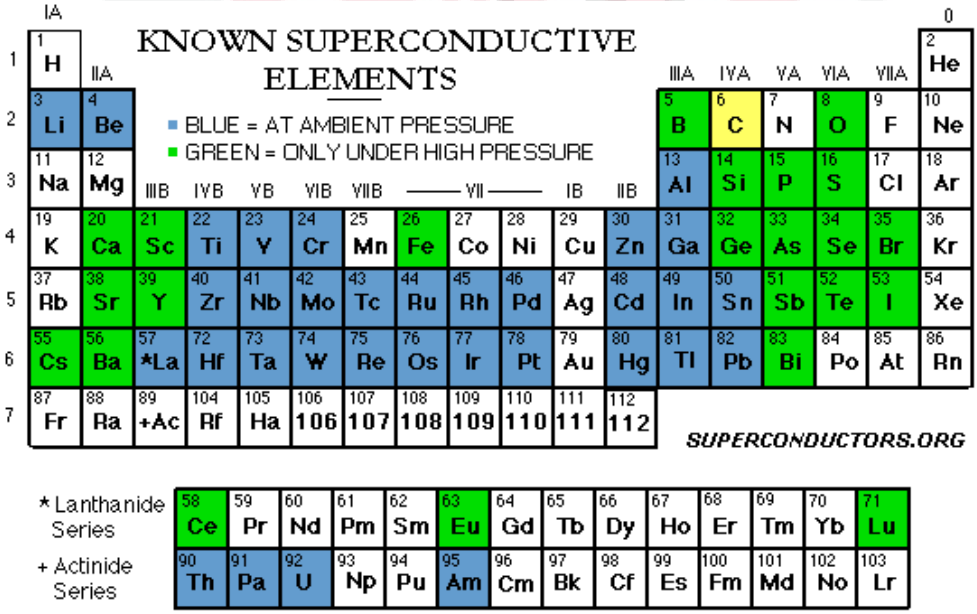

Figure 2.2: Every elemental superconductor that has ever been discovered are included in the periodic table where the blue colour stands for the element that can experience a superconductive state at ambient pressure while the green colour showed the elements that require high pressure to undergo a superconducting state (Resources from ffden-2.phys.uaf.edu).

2.2.1 Type-I Superconductors

Type-I superconductors are usually metals and metallic alloys that are electrical conductors at room temperature and develop superconductive properties at very low temperatures. Mercury (Hg) is the first element that had a zero resistivity when applying 4.2 K and physicist Heike Onnes discovered it in 1911 (Roque et al., 2017). Superconductors are more likely with a specific critical temperature and the state will be changed abruptly. Type-I superconductors are known when it possesses the Meissner effect completely. It has zero electrical resistance below a critical temperature, zero internal magnetic field, and a critical magnetic field above which superconductivity ceases (Bharat, 2018).

In addition**,** type I superconductors are mostly used in various fields from electrical cabling until microchips on the devices and known as low temperature superconductors (LTS). This class of superconductor contains basic conductive components and when it is inserted into a magnetic field, type-I will easily lose it superconductivity. Due to the lack of superconductivity, this superconductor is identified as a "soft" superconductor and fully complies with the Meissner effect (Bharat, 2018). The example of type-I superconductor is aluminum and zinc. In Figure 2.3, the graph indicates that when a strong magnetic field is applied to the type-I superconductor materials and exceeds a critical value, superconductivity is abruptly destroyed by a first-order phase transition.

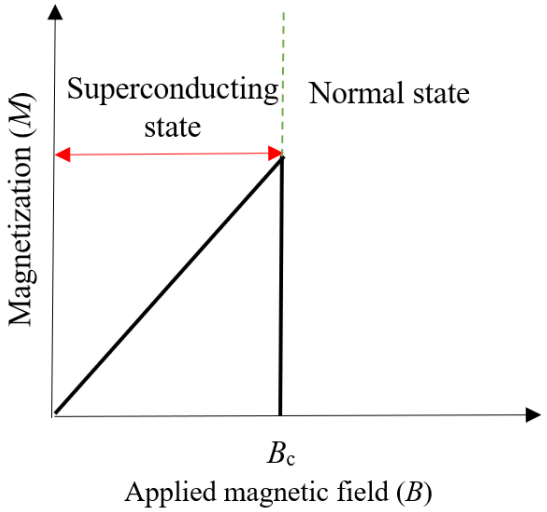

Figure 2.3: The magnetic flux is released from a type-I superconductor resulting a magnetization that increases with magnetic field (*B*) until a critical field (B_c) is achieved at which it falls to zero as with a normal conductor (Soyeon Shin, 2015).

2.2.2 Type-II Superconductors

Type-II superconductor is acclaimed as High Temperature Superconductor (HTS) where it requires high temperature to become superconductive. Besides, this class of superconductor are efficient of hauling massive currents in the presence of strong magnetic field without any dissipation of energy and thus, it is making them one of the technologically significant (Wesche, 2015). This type-II is commonly known as “hard” superconductors and it partially obey the Meissner effect. The excellent example of this type II superconductor is NbN, which is exclusively used in superconducting magnets with a high field strength.

Besides, type-II superconductors are unique in the way that they occur in mixed state of normal and superconducting states, as shown in Figure 2.4. This is frequently referred to as the vortex state because vortices of superconducting current surround filaments or cores of conventional material. Furthermore, the superconductors in this class do not have a sharp transition change compared to type-I superconductors (Bharat, 2018). Metallic alloys and

other substances mostly form type II superconductors. The pure metals Vanadium (V), Technetium (Tc), niobium (Nb), and carbon (C) are exceptions since they are Type-II superconductors (Roque et al., 2017). In addition, type-II superconductors have the formation of magnetic flux pass through into the materials in the presence of an applied magnetic field, which is described as a vortex. This phenomenon occurs initially above a critical field strength known as the lower critical field, B_{c1}. And as the field strength rises, so does the density of the vortex (Soyeon Shin, 2015).

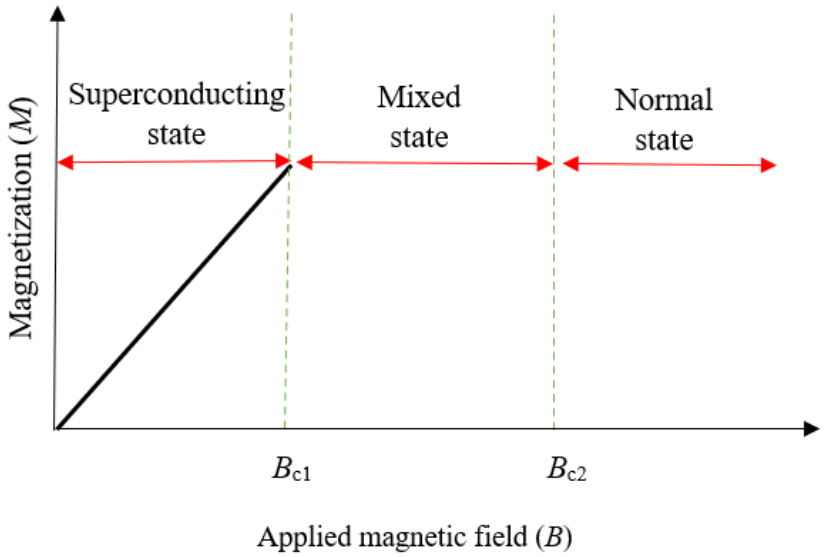

Figure 2.4: A type-II superconductor has two critical magnetic fields which are B_{c1} and B_{c2}. Below B_{c1}, the superconductor will behave like a type-II, and beyond B_{c2}, it will act like a normal superconductor (Soyeon Shin, 2015).

2.3 BCS Theory and Copper Pairs

The phenomenon of superconductivity could not be explained satisfactorily by classical physics theories for many years, however, in 1950s, John Bardeen, Leon Cooper, and John Schrieffer which an American Scientist developed a superconductivity theory that earned them the Nobel Prize in Physics in 1972. The theory that they are created was named after the first letters of their surnames as the BCS theory. Besides, the properties of type-I superconductor were described successfully by BCS theory with the effort from this American physicist. Based on the theory, electrons are able to flow through a material with zero resistance due to attractive interactions between two electrons that are distance apart (McQuarrie, 2013).

Furthermore, the basic aspect of BCS theory is when two electrons in the superconductor are potentially formed a bound pair named a Copper pair, when they experience an attractive interaction between them (Khachan & Bosi, n.d.). At first glance, this idea seems illogical because electrons generally repel one another due to their similar charges and this is visualized in Figure 2.5.

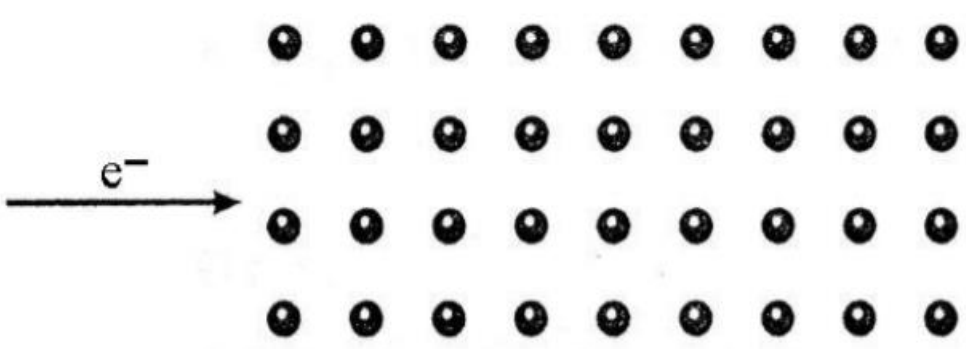

Figure 2.5: An electron approaching a section of the crystal lattice (Khachan & Bosi, n.d.).

It started when an atom is placed in a crystalline lattice where it vibrates slower as it falls below the critical temperature. Once the electron enter the crystal lattice, the atoms surrounding it are attracted due to the electron is negatively charged while the atom is positively charged distorting the lattice which known as a phonon electron interaction. This event occurs as shown in Figure 2.6. As electrons flow through a lattice, this somehow will distort it. If another electron enters the lattice, it is pulled to the distortion caused by the first electron. Note that, the second electron is driven to the distortion generated by the first electron rather than the first electron itself. Therefore, this will form a weak link between these two electrons, where these two electrons are linked somehow, and this is referred to as a Copper pair. Thus, as the first electron travels through the lattice unhindered, the distortion occurs and it drags the second electron where this is explains how a material can be very superconductive. Fundamentally, the BCS theory results from a mild delayed attractive force between the two electrons (Khachan & Bosi, n.d.).

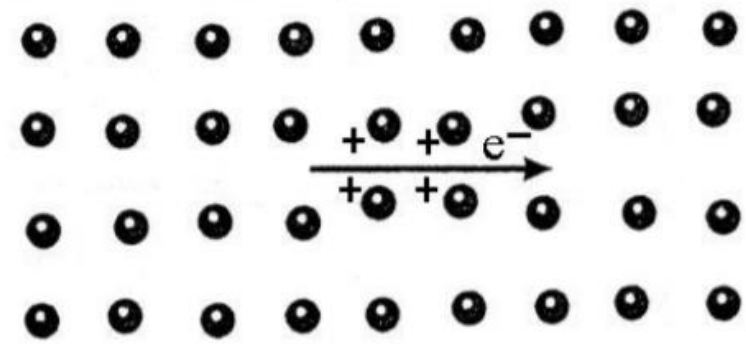

(a)

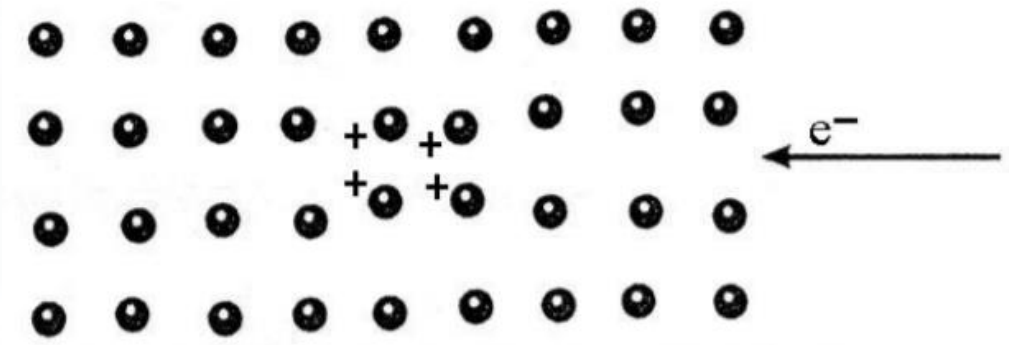

(b)

Figure 2.6: (a) An electron deforms part of the lattice electrostatically and (b) the second electron is attracted to the net positive charge of the deformation (Khachan & Bosi, n.d.).

2.4 Yttrium Barium Copper Oxide System (YBCO)

Paul Chu and his colleagues found the discovery of material YBa2Cu3O7 or often shortened to YBCO-123 in 1987. This material had an extremely high superconductivity transition temperature, T_c of approximately 92 K and it is over a liquid nitrogen barrier (77 K), making it relatively easy to synthesis. The history of the discovery in superconducting material is visualized in Figure 2.7. The crystalline structure of $YBa_2Cu_3O_7$ has features orthorhombic structure symmetry with two cooper-oxygen planes and oxygen chains along the b-axis (Saxena, 2009). In Figure 2.8, B represents the metallic cation Cu (small radius), surrounded by six oxygen ions and will fill site X. In contrast, yttrium will occupied the metallic cation site A. Therefore, the structure can be portrayed as perovskite with a lack of oxygen. Thus, removing the oxygen atom from the ideal perovskite lattice will acquire the $YBa_2Cu_3O_{7-\delta}$ compound (Saxena, 2009).

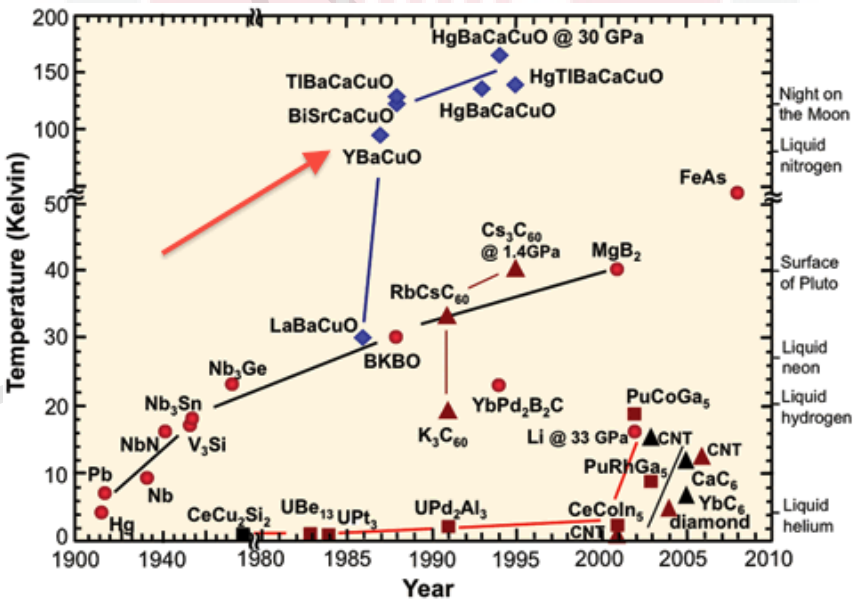

Figure 2.7: This chronology of superconducting material discovery reveals how significant the finding of high-Tc YBCO was (Resources from physicsforme.com).

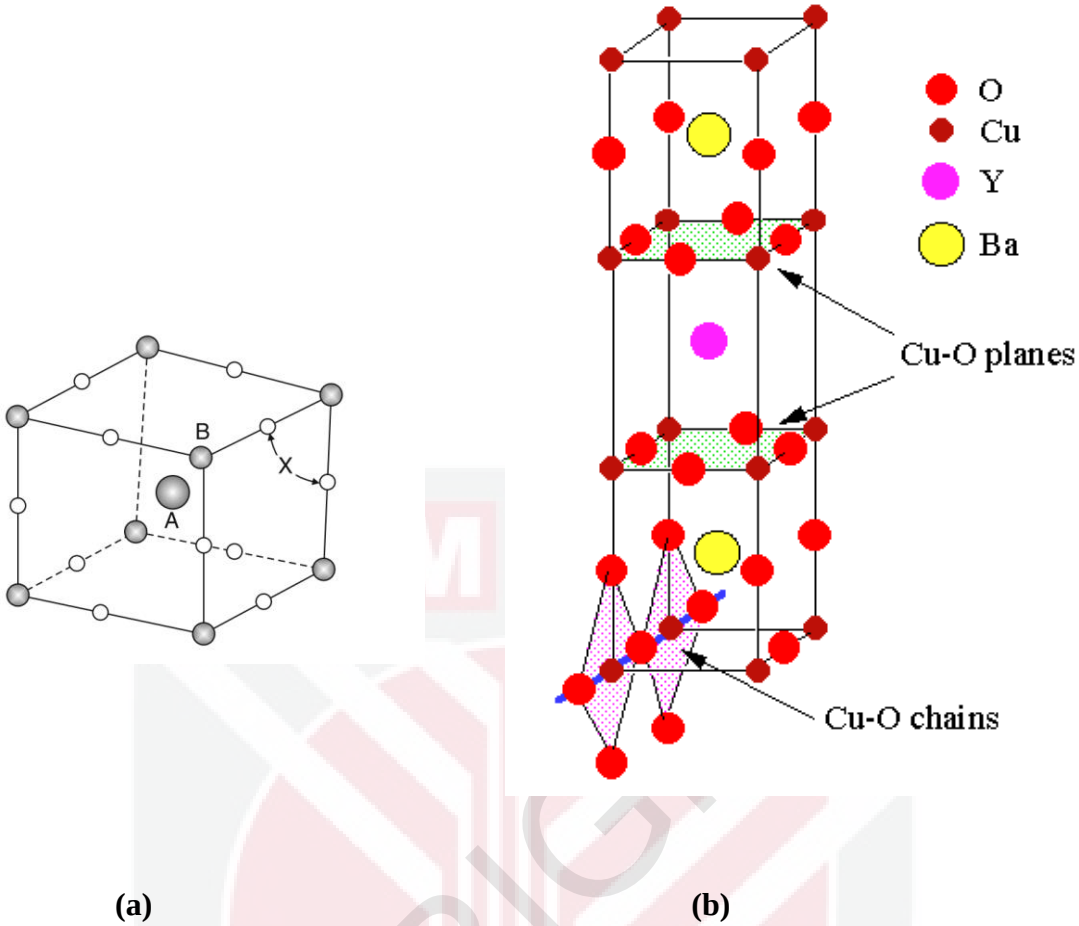

Figure 2.8: (a) The perovskite structure ABX_3 (Saxena, 2009) **and (b) The crystal structure of $YBa_2Cu_3O_7$ (Zhou, 2019).**

The Cu is located in the unit cell's corner and has two different co-ordinates with regard to oxygen, Cu(1) and Cu(2). The triple of the perovskite unit cell tends to produce 9 oxygen atoms, however the $YBa_2Cu_3O_7$ (YBCO) yields 7 oxygen atoms which indicating that the perovskite structure is lack of oxygen (Gopalakrishnan et al., 1987). The YBCO unit cell has two layers of CuO_2 which approximately ~ 3.2 Å (Dagotto, 1994). Hence, the crystal structure is orthorhombic when the critical temperature is about 90 K with x approximate to 0.16. When the superconductivity occurs at x= 0.6, the YBCO structure transforms from orthorhombic to tetragonal. YBCO crystal structures of lattice parameters are a = 3.82 A°, b

= 3.89 A°, and *c* = 11.67 A°, where two Cu-O sheets in the ab plane (Prabhakar & Wani, 2020). The orthorhombic $YBa_2Cu_3O_7$ structure is formed by oxygen atoms parallel to the a-axis at the Z= 0 and Z= 0.5 levels of the stoichiometric perovskite (Prabhakar & Wani, 2020).

2.5 Advantages Of Thermal Treatment Method

Over years, all the scientist across the globe is constantly working on the different methods developed to prepare superconducting powder to enhance the efficiency and cost-effectiveness of these procedures. All types of preparation methods aim to produce a pure, homogenous, dry product with the fewest contaminants as possible (Maric, 1991). However, the technique that can be used to prepare superconducting powder such as sol-gel, thermal decomposition, sonochemical method and laser ablation may be dangerous due to these processes rely on intricate handling processes, long reaction times, and harmful chemicals, and it can create hazardous by-products, making them unsuitable for large-scale manufacturing (P. J. Lee et al., 2015).

Thus, the thermal treatment method is a method that help to promote the preparation of nanoparticles where; this approach is favourable because of its simplicity and it is environmentally friendly since it does not require harmful reagents or create hazardous by-products (P. J. Lee et al., 2015). Moreover, this method has the advantages of simple step, low cost and containing a superfine powder.

Chapter 3

METHODOLOGY

3.1 Overview

This chapter will discuss the preparation method of Y-123 powder by using a thermal treatment method that involves chemical substances, processes, and characterization of the samples.

In the overview, the diagram in Figure 3.1 showed the flow of the preparation of Y-123 powder with the same sintering condition but different in temperature. The sample will be characterized by using various techniques such as:

1. Thermogravimetric Analyzer (TGA)

   This characterization is used to determine the sample's thermal stability (weight changes). The temperature range for this instrument is from room temperature up to 1000°C.

2. X-ray diffraction (XRD)

   This characterization is used to determine the phases present in the sample, its crystal structure, the orientation of grain growth, and the crystal size.

3. AC Susceptibility (ACS)

   This characterization is to determine the critical temperature T_c.

4. Scanning Electron Microscopy (SEM)

   This characterization is to determine the surface morphology of Y-123 superconductor as well as its grain size.

5. Four Point Probe (4PP)

   This characterization is to measuring the resistivity of samples. The substrate resistivity can be measured by passing current through two outer probes and measuring voltage through the inner probes.

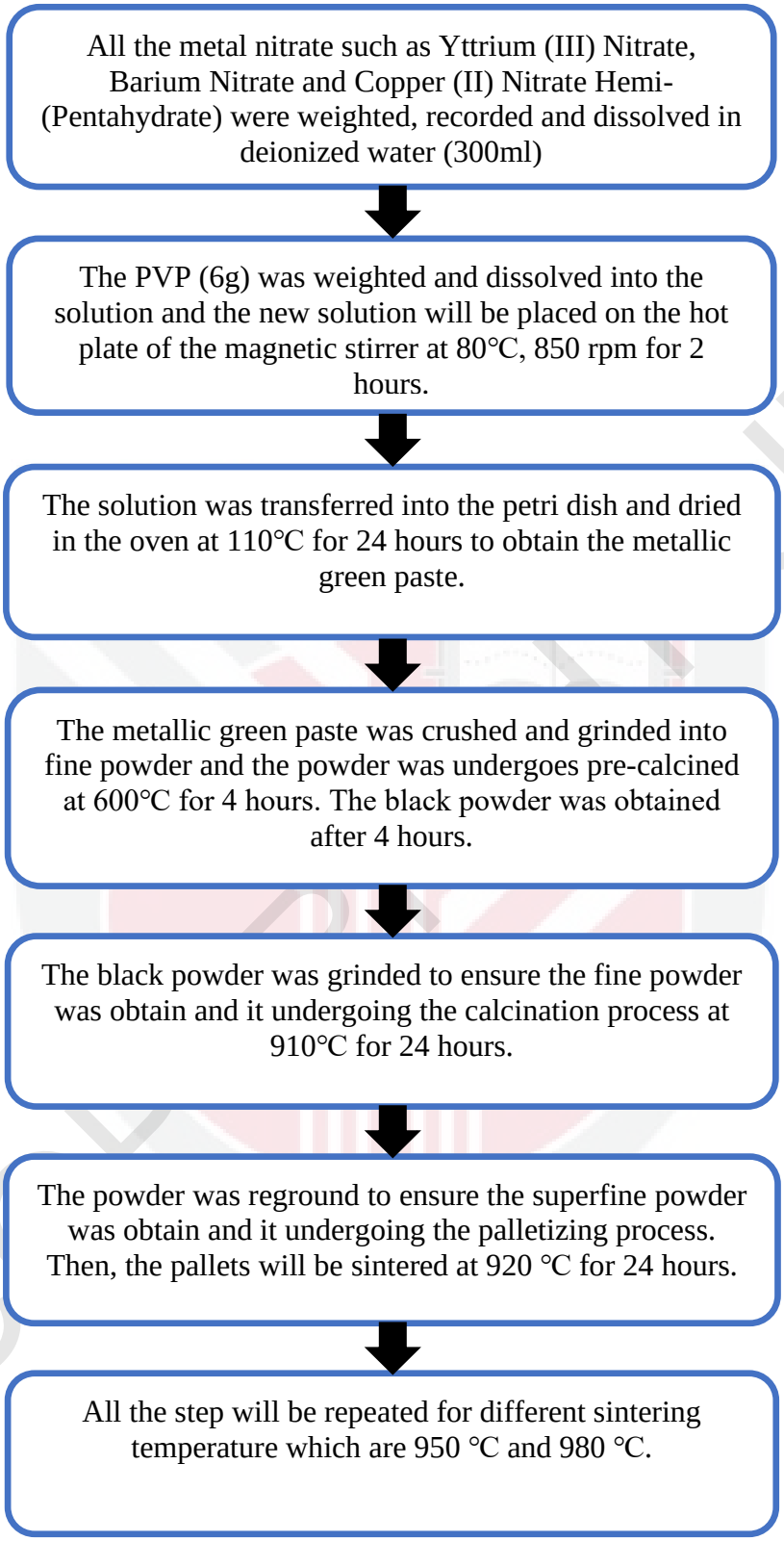

Figure 3.1: Flow Diagram of Sample Preparation at 920 ℃, 950 ℃ and 980 ℃ temperatures.

3.2 Preparation of Sample of Y-123

In this research, the sample of Y-123 was prepared by using the thermal treatment method. Metal nitrate such as Yttrium (III) Nitrate, Barium Nitrate and Copper (II) Nitrate Hemi-(Pentahydrate) were the major substances used in the sample preparation. Table 3.1 shows the atomic mass of each element in the mixture.

Table 3.1: The atomic mass of each element in the YBCO compound

Element	Atomic Mass (g/mol)
Y	88.9054
Ba	15.9994
Cu	63.5460
O	15.9994
N	14.0067
H	1.0079

3.2.1 Apparatus and Materials used for sample preparation of YBCO

Several apparatus such as digital balance, magnetic stirrer, spatula, weighing paper and measuring cylinder used for thermal treatment method to mix all the precursor for the sample preparation of YBCO. Next, the other apparatus supporting this method in the heat treatment process are petri dish, crucible, alumina boat, oven, box furnace, tube furnace, mortar and pestle . At the same time, the hydraulic press and set of palletization mouldwere also used to obtain a valuable powder during the grinding process. In contrast, the hydraulic press and palletization mold was used in the palletization process.

Besides, the materials that used in this research are Yttrium (III) Nitrate, Barium Nitrate, and Copper (II) Nitrate Hemi-(Pentahydrate). Polyvinyl Pyrrolidone (PVP) was added to this research and it is act as a capping agent to coat the nanoparticle. The materials used in the research were supplied by Alfa Aesar company and shown in Figure 3.2.

(a)

(b)

(c)

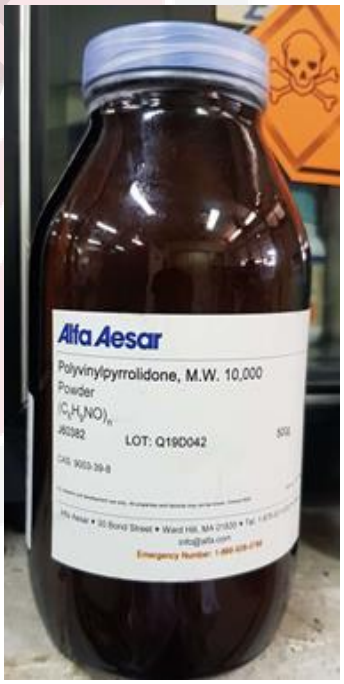

(d)

Figure 3.2: The chemical substances used in preparing sample (a) Yttrium (III) Nitrate (b) Barium Nitrate (c) Copper (II) Nitrate Hemi-(Pentahydrate) and (d) Polyvinyl Pyrrolidone (PVP).

3.2.2 Calculation of Chemical Mole Ratio for YBCO Sample

Essentially, nitrate was utilized as a base chemical in the thermal treatment method in order to create pure Y-123 samples. The samples consisting of $Y(NO_3)_3.6H_2O$, $Ba(NO_3)_3$ and $Cu(NO_3)_2.2.5H_2O$ with high purity (99.9%) represent as main chemical substances. Moreover, the mixture of polymer like Polyvinyl Pyrrolidone (PVP), (C6H9NO)n is influential in this method since it can act as the capping agent. Table 3.2 showed the amount of chemical substances used to synthesize Y-123 calculated based on the numbers of their moles: Y: Ba: Cu = 1: 2: 3. Next, Table 3.3 showed the mass of Polyvinyl Pyrrolidone (PVP) in 2% aqueous solution. The purpose of this calculation is to prepare 10 grams of compound mixture of Y-123.

Table 3.2: Calculation for the mass of chemical materials used to prepare 10g of Y-123.

Chemical Materials	Mole Ratio	Molar Mass (g/mol)	Weight Ratio (g/mol)	Weight for 10 g
$Y(NO_3)_3.6H_2O$	1	383.0113	383.0113	2.3886
$Ba(NO_3)_3$	2	261.3368	522.6736	3.2596
$Cu(NO_3)_2.2.5H_2O$	3	232.5938	697.7814	4.3518
Total			1603.4663	10.0000

Table 3.3: Calculation for the mass of Polyvinyl Pyrrolidone (PVP) in 2% aqueous solution used to prepare 10g of Y-123.

Chemical Materials	Ratio	Ratio for 10 g
$(C_6H_9NO)_n$	2 g	6 g
Deionized water	100 ml	300 ml

3.3 Procedure

3.3.1 Thermal Treatment Method

The sample preparation process is started by cleaning all the required apparatus during the experiment to refrain any impurities that will affect the result of the sample. Spatula, beaker, measuring cylinder, magnetic stirrer, crucible, alumina boat, mortar and pestle were then rinsed with water followed by acetone to make it quick in drying process. The next step is, all the chemical materials such as $Y(NO_3)_3.6H_2O$, $Ba(NO_3)_3$, $Cu(NO_3)_2.2.5H_2O$ and Polyvinyl Pyrrolidone (PVP) was weighed by using the digital balance and the quantity for each material must be followed as stated in Table 2 and Table 3. Then, by using a measuring cylinder, 300ml of deionized water was measured and placed into a beaker where all the weighed chemical materials are in a beaker in which all the weighed chemical materials would dissolve.

Next, the beaker was then positioned on the magnetic stirrer, which was then covered with aluminium. Then, the magnetic stirrer was set with 850 rpm at 80 ℃ and this process will be carried out for 2 hours to ensure the entire compound was mixed until the blue solution turns to the light green solution. The green solution will be inserted into the oven at 110 ℃ for 24 hours to let the drying process take place to obtain the powder where the color is green as shown in Figure 3.3.

Figure 3.3: The light green solution was placed in a petri dish and inserted into oven at 110 ℃ for 24 hours.

3.3.2 Calcination

After completing the drying process in the oven, the dark green lump was obtained as shown in Figure 3.4. Then, the dark green lump in the petri dish was crushed and transferred into mortar to continue the grinding process until turned into fine light green powder, as demonstrated in Figure 3.5. The pre-calcination process begins when the light green powder is put into alumina cup which covered with an alumina crucible and placed in the box furnace at 600 ℃ for 12 hours. Finally, the graph of the pre-calcination process is provided as shown in figure 3.6.

Figure 3.4: The dark green powder obtained after the drying process was undergone in the oven at 110 ℃ for 24 hours.

Figure 3.5: The light green fine powder obtained after the grinding process.

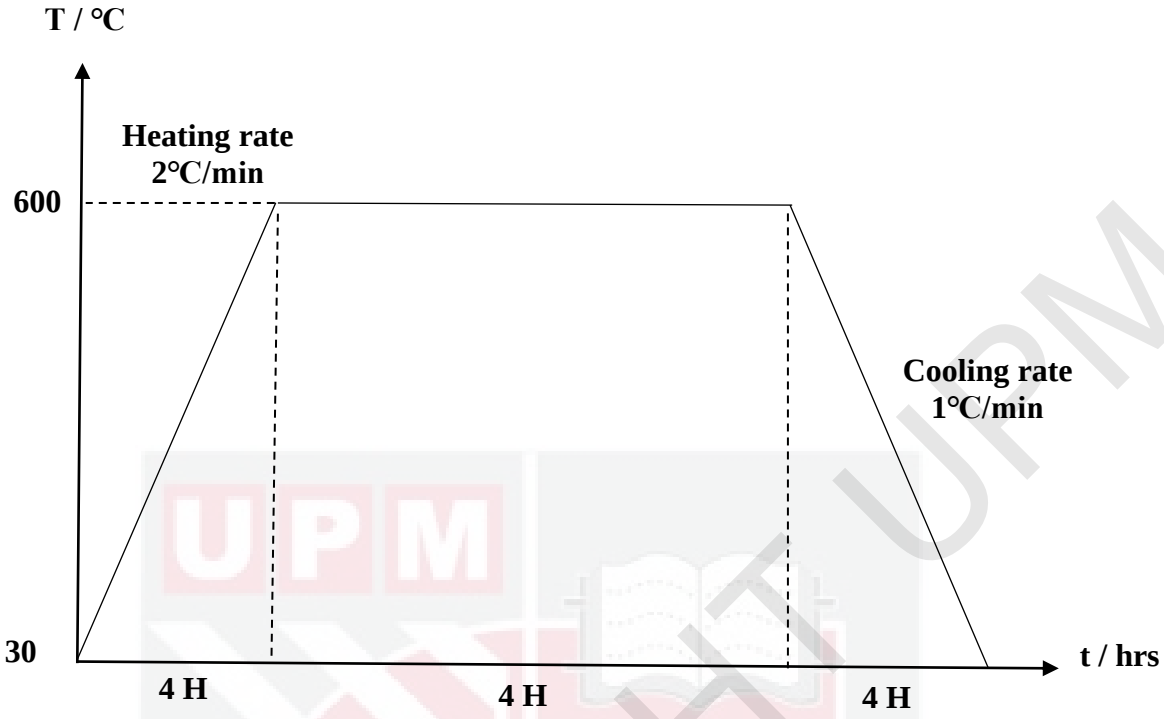

Figure 3.6: Pre-calcination with heating and cooling curve for 4 hours process. Hour starts with 4, 8, 12

Next, the result of light green powder after undergoing the pre-calcination process will transform into black powder with the texture of the powder similar to the dust as shown in figure 3.7. The powder was then ground again to ensure that the superfine powder could be collected and was placed into an alumina boat to experience the calcination process. The graph of calcination process was illustrated in figure 3.8. The calcination process was set up at 910 ℃ for 24 hours by using double tube furnace. Subsequently, the process of grinding was repeated once again to obtain the fine powder. In addition, the calcination process is necessary to help in removing unwanted volatile materials and allow the decomposition of Polyvinyl Pyrrolidone (PVP) and nitrates is leaving where only YBCO elements exist in the sample.

Figure 3.7: The black powder formed after pre-calcination process and the powder was grinded once again to ensure the finest powder can be obtained.

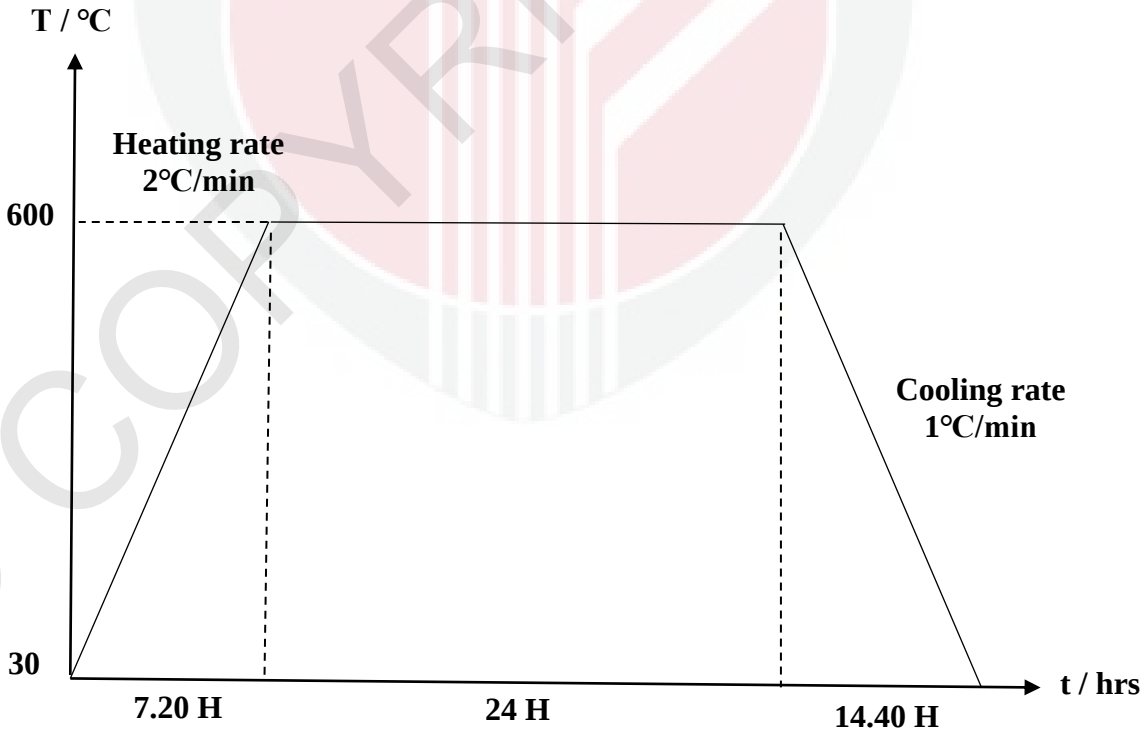

Figure 3.8: Calcination with heating and cooling curve for 24 hours process.

3.3.3 Palletization

Palletization is the process where the fine powder will be compacted into solid form known as pellet**.** During this process, the pellet was created by inserting the powder that was obtained during the calcination process into mold and pressing it with a hydraulic presser. But before the process of pelletization begin, the powder will be ground for 1 hour to make sure only a very fine powder was inserted into the mold. The mold and hydraulic presser must be appropriately cleaned before using it to prevent any contamination that may have an impact on the outcome. Then, the mold was pressed with 5 tons of pressure and wait for it for 5 minutes before carefully releasing the pressure to avoid any crackdown on the pellet. The palletization process will be repeated if there any crackdown on the pellet during the pellet was taken out. Figure 3.9 shown the pellets obtained after taken out from the mold.

Figure 3.9: Four pellets which 1 gram each were obtained after compressed with pressure at 5 tons.

3.3.4 Sintering

The sintering process is the final part in preparing pure Y-123 samples. This process aims to enhance component metal interdiffusion to form the required crystal structure by heating the pellet below the melting point. To achieve the objective of this research, a different sintering temperature was applied during this process. The sintering process was started by setting the temperature at 920 ℃, 950 ℃ and then continued at 980 ℃. The graph of the sintering process was shown in Figure 3.10 for temperature at 920 ℃, Figure 3.11 for temperature at 950 ℃ wheras Figure 3.12 for temperature at 980 ℃.

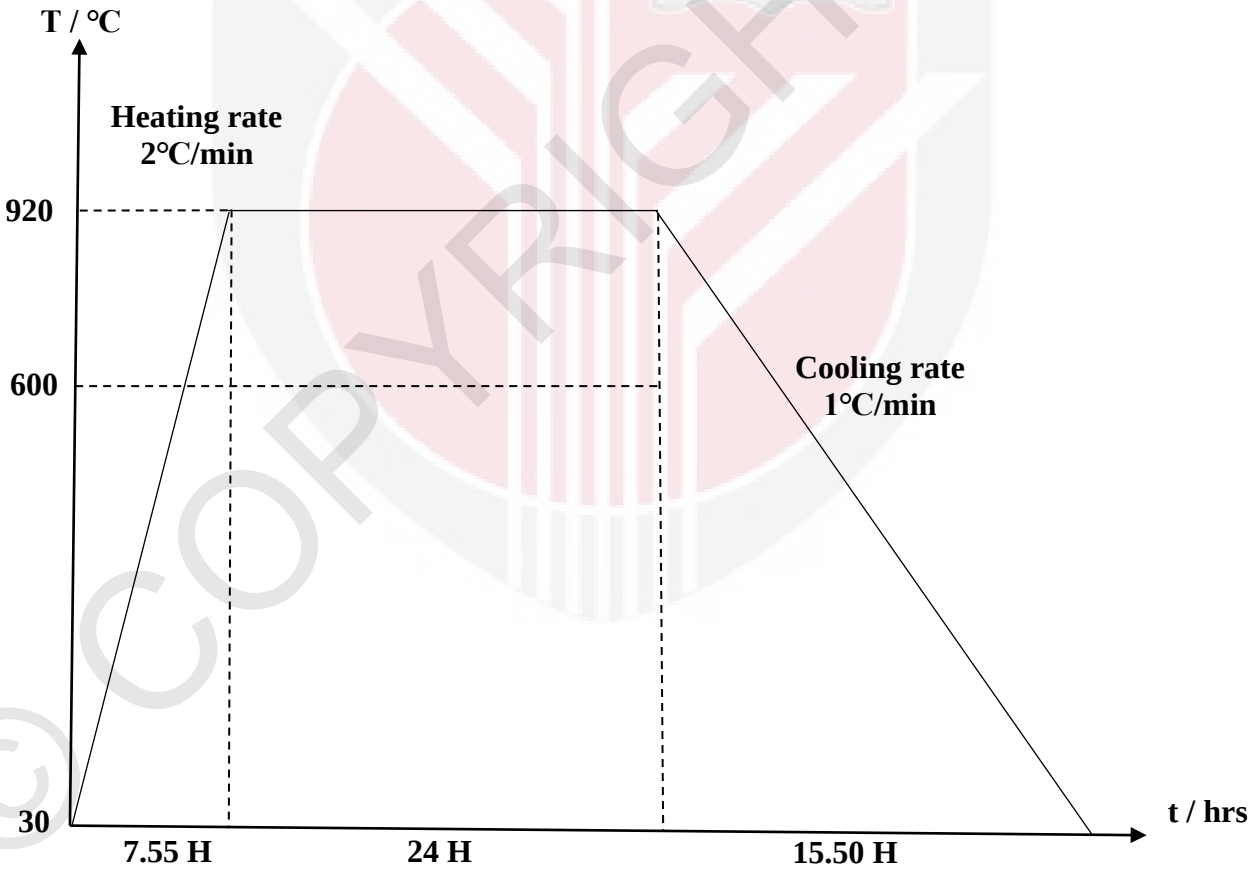

Figure 3.10: Sintering process at 980 ℃ with heating and cooling curve for 24 hours process.

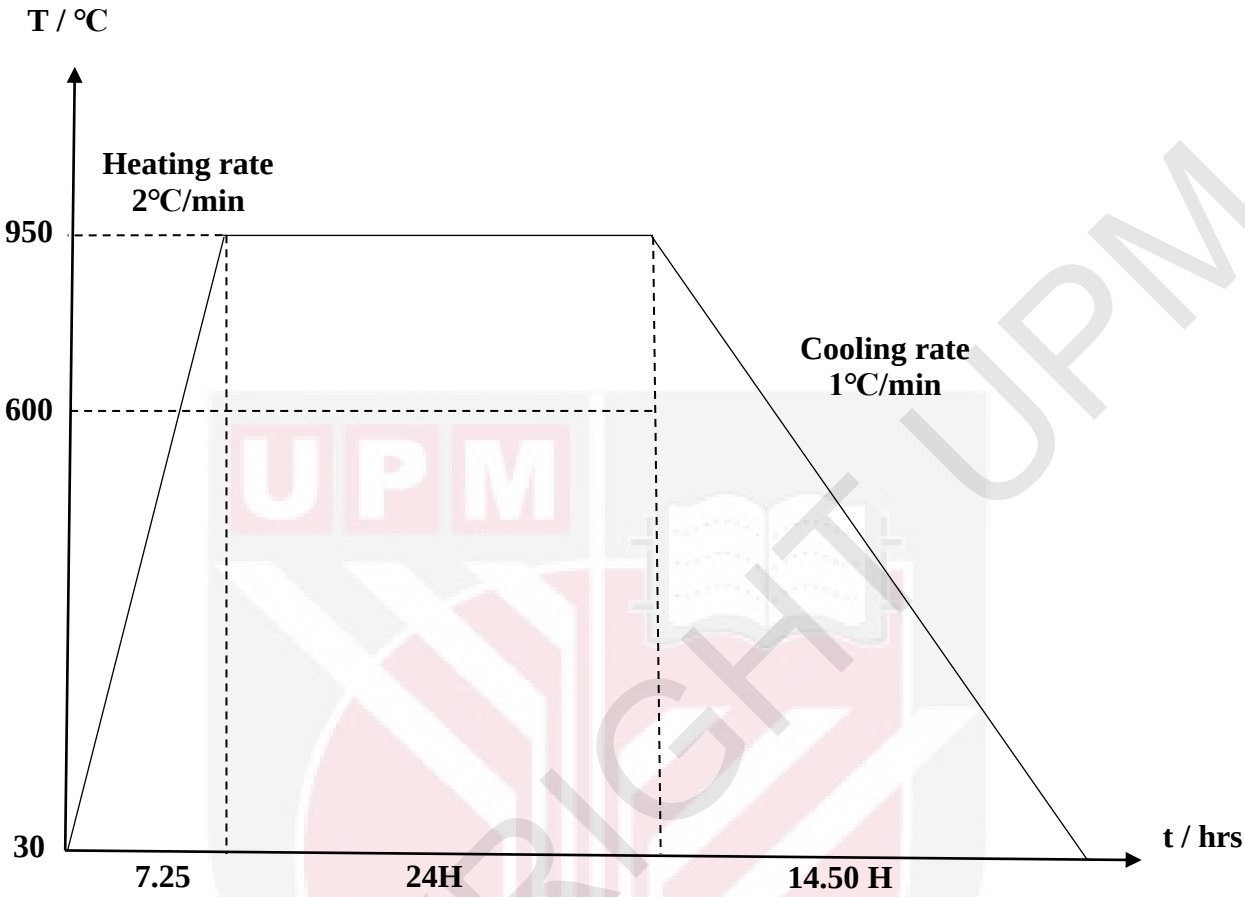

Figure 3.11: Sintering process at 950 °C with heating and cooling curve for 24 hours process.

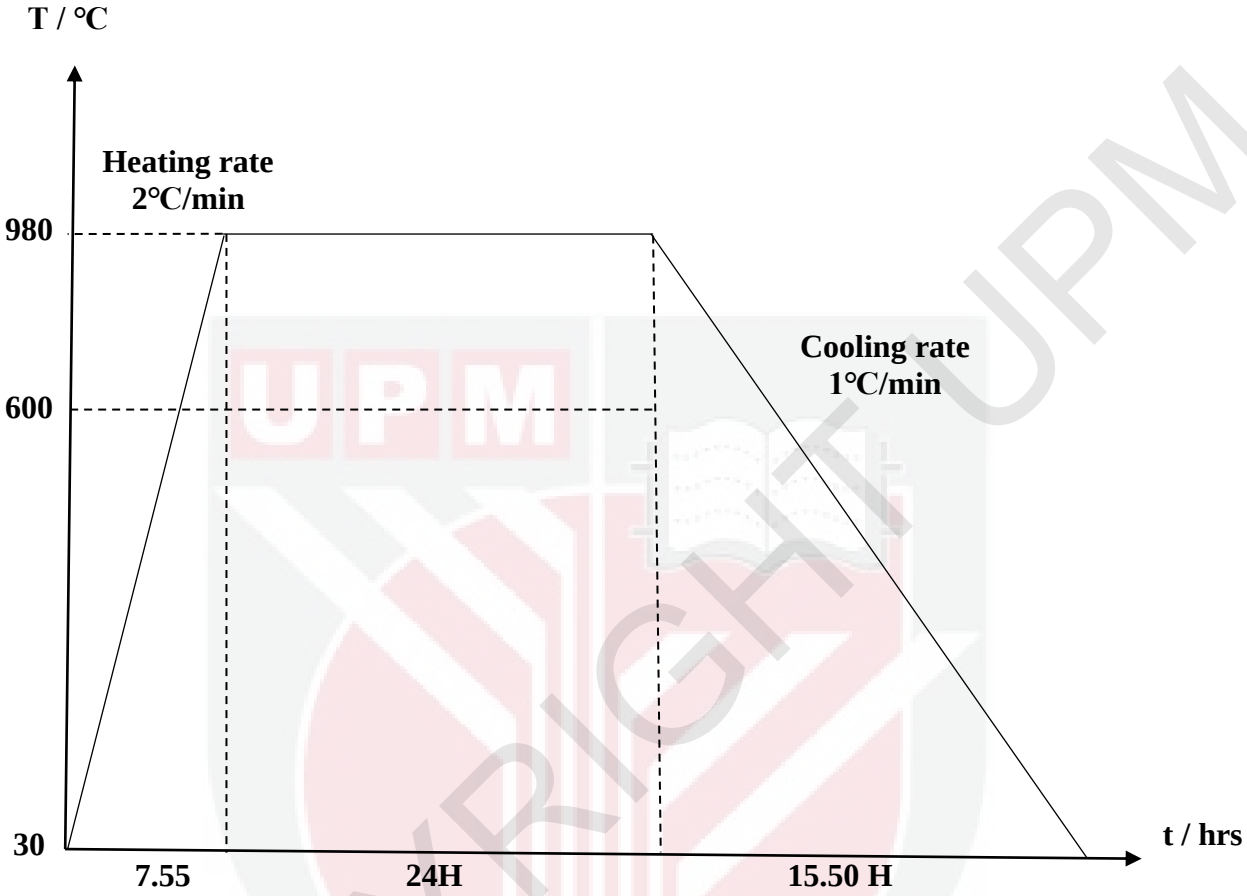

Figure 3.12: Sintering process at 920 ℃ with heating and cooling curve for 24 hours process.

3.4 Characterization

In this research, all the sample were characterized by using Thermogravimetric Analyzer (TGA), X-ray diffraction (XRD), AC Susceptibility (ACS), Scanning Electron Microscopy (SEM) and Four Point Probe (4PP) where each of these instruments will function differently.

3.4.1 AC Susceptibility (ACS)

The AC susceptibility or AC susceptometer is the dynamic magnetic susceptibility technique where it is a very sensitive and underutilised approach tool for characterising materials (Ba[a]anda, 2013). In the static (DC) magnetic field, the measurement of AC susceptibility is complementary and it became crucial for studies of phase transition and magnetic relaxation. However, in physics, this instrument is the standard tool for determining superconductors, specifically critical temperature (Martien, n.d.). Superconductors often have a low susceptibility above the critical temperature and at superconducting state, the sample is a perfect diamagnet which $\chi' = -1$. Generally, the start of a significant nonzero χ' is commonly used as the superconducting transition temperature.

The component of AC susceptibility consists of two sets of circular coils which is primary and secondary. The function of primary coils is to generate the magnetic field whereas the role of secondary coil is in inducing and measuring voltages. These two sets of coils are made up of two in-series coils coiled in different directions within the primary coil. When an AC is supplied to the primary coils, an oscillating flux is generated through secondary coils. This will lead to an equal and opposite voltage produced in each of the two coils by cancelling out and resulting in 0 volts detected across the whole secondary circuit. Figure 3.13 shows the schematic diagram of the primary and secondary coil arrangement.

Thus, AC susceptibility measurements have helped find crucial indices related with the second order para-to ferromagnetic phase transition (Drobac, 1996).

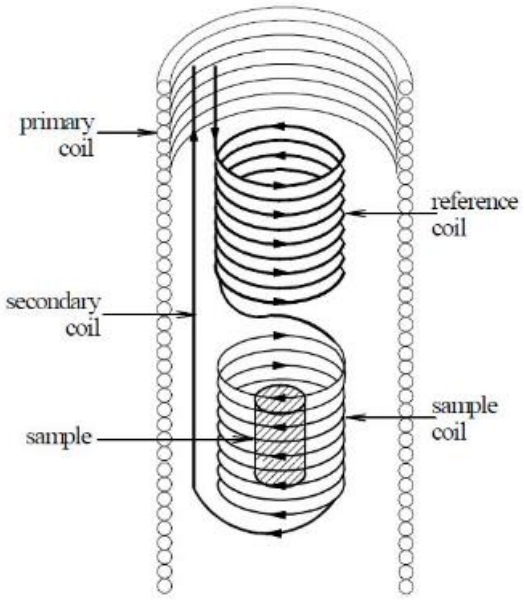

Figure 3.13: The component of susceptometer which including the primary and secondary coil. For the secondary coil, it consisting of reference coil at the top and sample coil at the bottom (University of Florida, 2003).

3.4.2 X-Ray Diffraction (XRD)

X-ray diffraction (XRD) is a non-destructive method for obtaining precise information on a material's crystallographic structure, chemical composition, and physical characteristics (Vishwakarma & Uthaman, 2020). The Brag Brentano technique will be used for this instrument in order to evaluate and identify unknown crystalline substances. X-ray diffractometers are three fundamental components: an X-ray tube, a sample holder, and an X-ray detector. In a cathode ray tube, X-rays are produced by burning a filament to produce electrons. The voltage was applied to the electrons, accelerating towards a target and hitting

the target material with electrons. Characteristic X-ray spectra are created when electrons have enough energy to displace inner shell electrons of the target material.

This method involves passing x-ray beams through it due to the wavelength of X-ray beams is equivalent to the gap between atoms in the sample. Therefore, the diffraction of angle will be impacted by the gap of the atoms in the molecule compared to use much greater wavelengths where it would be unaffected by the distance between atoms. The x-ray then travels through the sample, triggered the atom and altering the direction of the beam at a new angle, θ, from the initial beam. A few of these diffracted beams will cancel out each other, but constructive interference occurs when the wavelengths of the beams are identical. In addition, two x-ray beams of the same wavelength will combine to form a new beam with a larger amplitude called as constructive interference, as shown in Figure 3.14. The bigger the wave's amplitude, the higher the signal for this precise angle of diffraction. By using Bragg's equation:

$$n\lambda = 2d \sin \theta \quad (1)$$

where;

n = order of diffraction

λ = the wavelength of x-ray

d = interplanar spacing of crystals

θ = diffraction angle

the angle of diffraction can be calculated through the difference between atomic plane. The gap between the atomic plates can be applied to compute composition or crystalline structure.

Thus, the crystalline phases and orientation of prepared samples was analysed by using X'Pert Graphics whereas identify it with CuK_a (λ = 1.5406 Å) in the 2θ range of 20° to 80°.

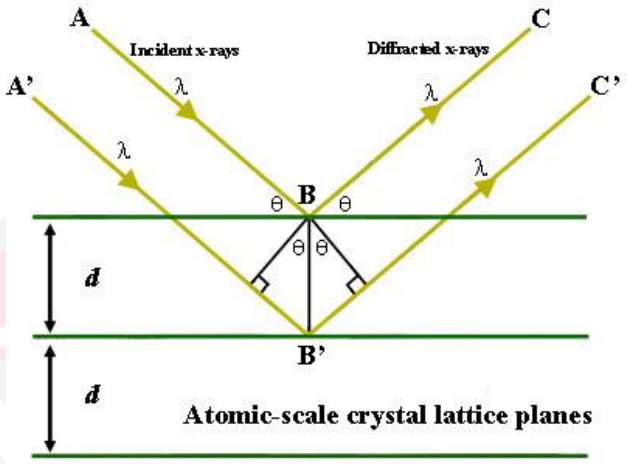

Figure 3.14: The reflection of Bragg's Law. When the distance between lines ABC and A'B'C' varies by an integer number of wavelengths (λ), the diffracted X-rays produce constructive interference (Resources from serc. carleton.edu).

3.4.3 Scanning Electron Microscopic (SEM)

Scanning electron microscope (SEM) generates a variety of signals at the surface of solid objects by using a focussed beam of high-energy electrons. The electron beam incident is scanned over the sample's surface in a raster pattern, and the second electrons emitted are identified (Khare et al., 2019). If a cathode releases the electrons in the presence of a very strong electric field known as field emitter (FE-SEM), it will produce the superior pictures. Besides, the electron beam might induce biological material deterioration even though the sample preparation is very straightforward and thus, it can be only utilised for restricted samples.

The main components of Scanning electron microscope (SEM) is a source of electrons, column down which electrons travel with electromagnetic lenses, electron detector, sample chamber, computer and display to view the images. All of these components can be seen in the Figure 3.15. This instrument started to work when an electron gun released an electron beam. Next, the electron beam will be reduced to a diameter of around 0.4-5 nm by using one or two condenser lenses. The beam is then deflected in the x and y axes by a pair of deflection coils in the electron column before interacting with the sample (Emily Nagle, 2019).

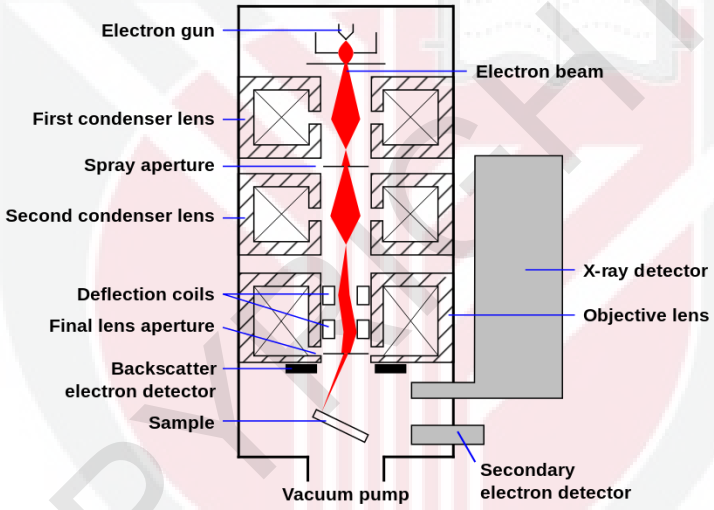

Figure 3.15: The schematic diagram of how an SEM works (Resources from nanoscience.com).

3.4.4 Thermogravimetric Analyzer (TGA)

Thermogravimetric analysis, also known as thermal gravimetric analysis (TGA), is a type of thermal analysis in which changes in physical and chemical characteristics of materials are evaluated as temperature rises (Sarfraz et al., 2020). The main application of this instrument are determining thermal stability of a material, the polymer filler content, the moisture and solvent content, and the percent composition of components in a compound. A

TGA analysis is carried out by progressively increasing the temperature of a sample in a furnace where the weight is monitored on an analytical balance that kept outside of the furnace. In addition, TGA detects mass loss when a heat event results in the loss of a volatile component.

In thermogravimetric analysis (TGA), a sample is continuously weighted while heating an inert gas environment is passed over it. Most of the materials undergo reactions that result in the formation of gaseous byproducts where this formation will remove and the changes of the residual mass of the sample will be recorded (Luis F. Garcia-Herrera & Henry Price, 2020).

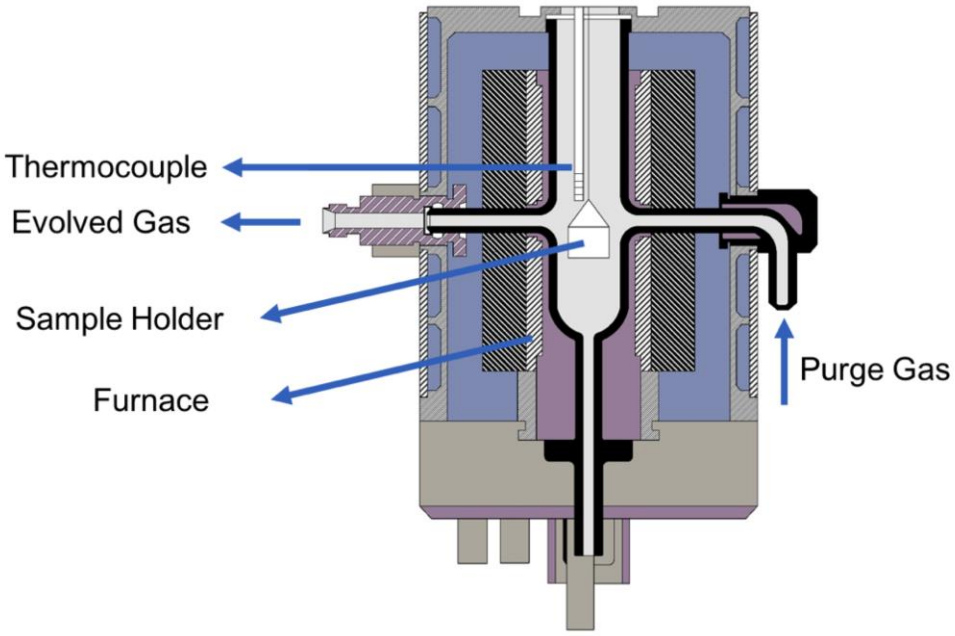

Figure 3.16: The major parts of a standard TGA instrument (Resources from cnx.org).

3.4.5 Four Point Probe (4PP)

The four point probe is a device that is typically used to assess or measure the resistivity value of a layer of electronic material. It is commonly used to evaluate the properties of semiconductor and thin-film materials (Waremra & Betaubun, 2018). As illustrated in Figure 3.17, a four point probe is made up of four electrical probes arranged in a line with equal spacing between them. The two outer wires were used to apply current to the material, while the two inner wires were used to measure voltage. As the temperature dropped, a small current was applied to the pellet sample, thus, the voltage change, V, was measured. Besides, Ohm's law was used to determine the resistance, R.

$$V = IR \qquad (2)$$

Where,

V = voltage across the wires,

I = the applied current

R = the resistance of the conductor

The graph temperature against resistance was obtained and the results was recorded from this tool. The onset superconducting transition temperature $T_{c\text{-onset}}$ is the temperature at which the resistance drops rapidly, and the resistance becomes non-linear as the temperature changes. However, The offset transition temperature, $T_{c\text{-offset}}$ is the temperature at which the resistance becomes zero. Thus, from the results, the graph will be plotted as normalized resistance against the temperature.

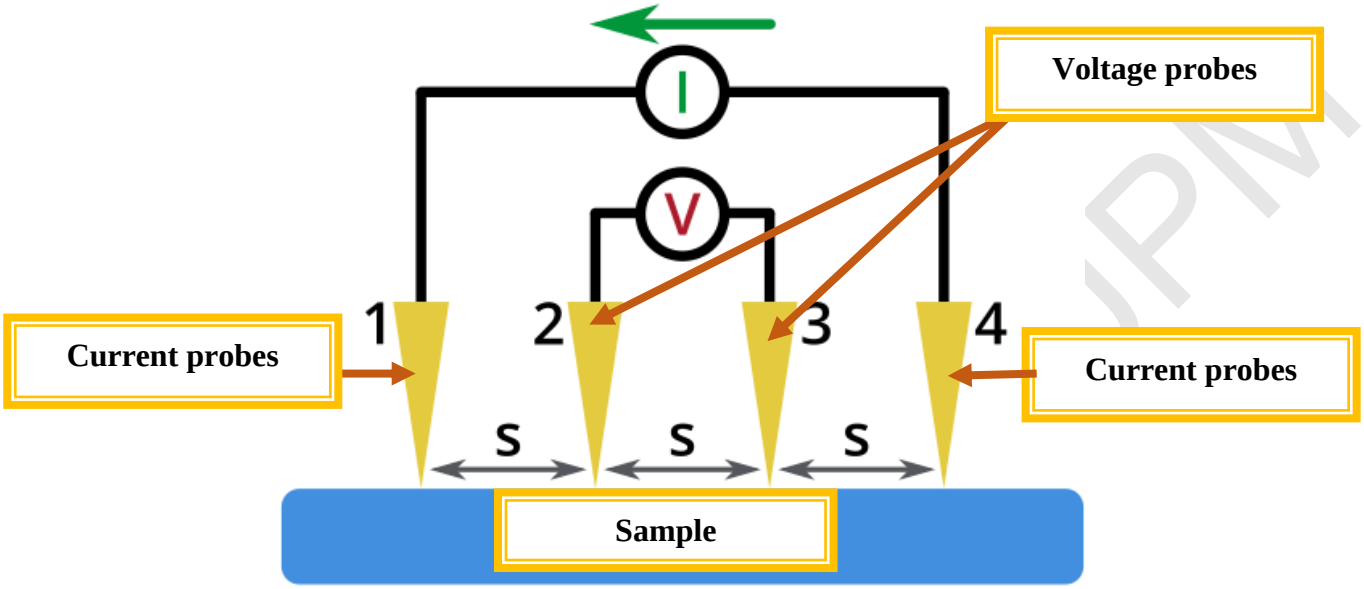

Figure 3.17: A four point probe is depicted in schematic form. The four point probe could be seen in contact with a surface and are spaced evenly. The voltage is measured between probes 2 and 3 whereas a current is supplied through probe 1 and received by probe 4 (Resources from ossila.com).

Chapter 4

RESULTS AND DISCUSSION

4.1 Introduction

This chapter will present and discuss more details about the results obtained by Thermogravimetric Analyzer (TGA), X-ray diffraction (XRD), AC Susceptibility (ACS), Scanning Electron Microscopy (SEM) and Four Point Probe (4PP). All of the data was gathered through sintering pure YBCO-123 at different temperatures for 24 hours, commencing with 920°C, 950°C, and 980°C. In this project, the sample was characterized to determine the formation of crystalline phases, surface morphology, and the surface structures.

4.2 Thermogravimetric Analyzer (TGA)

4.2.1 The influence of sintering temperatures on phase formation in TGA analysis.

The thermal decomposition of Y-123 precursor powder during TGA and DTG (derivative of the weight loss curve) measurements is depicted in Figure 4.1. Moreover, the temperature of thermal decomposition in this figure was revealed between 50 to 1000 ℃ which had been reported in a study that published in 2022 with some detailed information including nitrogen gas with a 5° / min scanning rate (Kamarudin et al., 2022).

In this sample, the thermal degradation process is observable in four drops. The initial drop shows 3.88% of weight loss at 60.41 to 325 ℃ and it could be seen clearly by the DTG measurements with the same temperature range as TGA (Ramli, 2015). This could be related to water and moisture loss throughout this drop. Hence, Kamarudin et al (2022) revealed that the weight loss was linked to water evaporation and moisture loss. Next, the second drop occurred at the temperature of 330 to 690 ℃ with the weight loss of 2.72%, as undesirable gases and organic compounds were eliminated. According to P. J. Lee et al (2015), at room temperature to 500 ℃, the sample lost over 77% of its mass because of trapped moisture under 100 ℃ and organic matter (PVP) below 460 ℃. Khoshnevisan et al., (2002), reported that, there was no weight change until the temperature reached 400 ℃ and later, another reaction were carried out (B. Khoshnevisan et al., 2002). Meanwhile, the next drop indicates a 1.46% weight loss of the sample when the temperature is increased from 700 to 870 ℃. This is due to the decomposition of every remaining volatile particle (Mousa Dihom et al., 2017). As explained by (Ramli, 2015), barium carbonate decomposes to barium oxide around 760 ℃ and at 896 ℃, it is fully decomposed. The fourth drop at the range of temperature 870 ℃ - 990 ℃ exhibited a weight loss of 1.97% attributed to the formation of the Y-123

structure has begun. A single crystal of Y-123 with an orthorhombic structure was formed at a temperature over 930 ℃ (Kamarudin et al., 2022). In summary, the range of pre-calcination, calcination and sintering temperature could be determined based on TGA and DTG measurements.

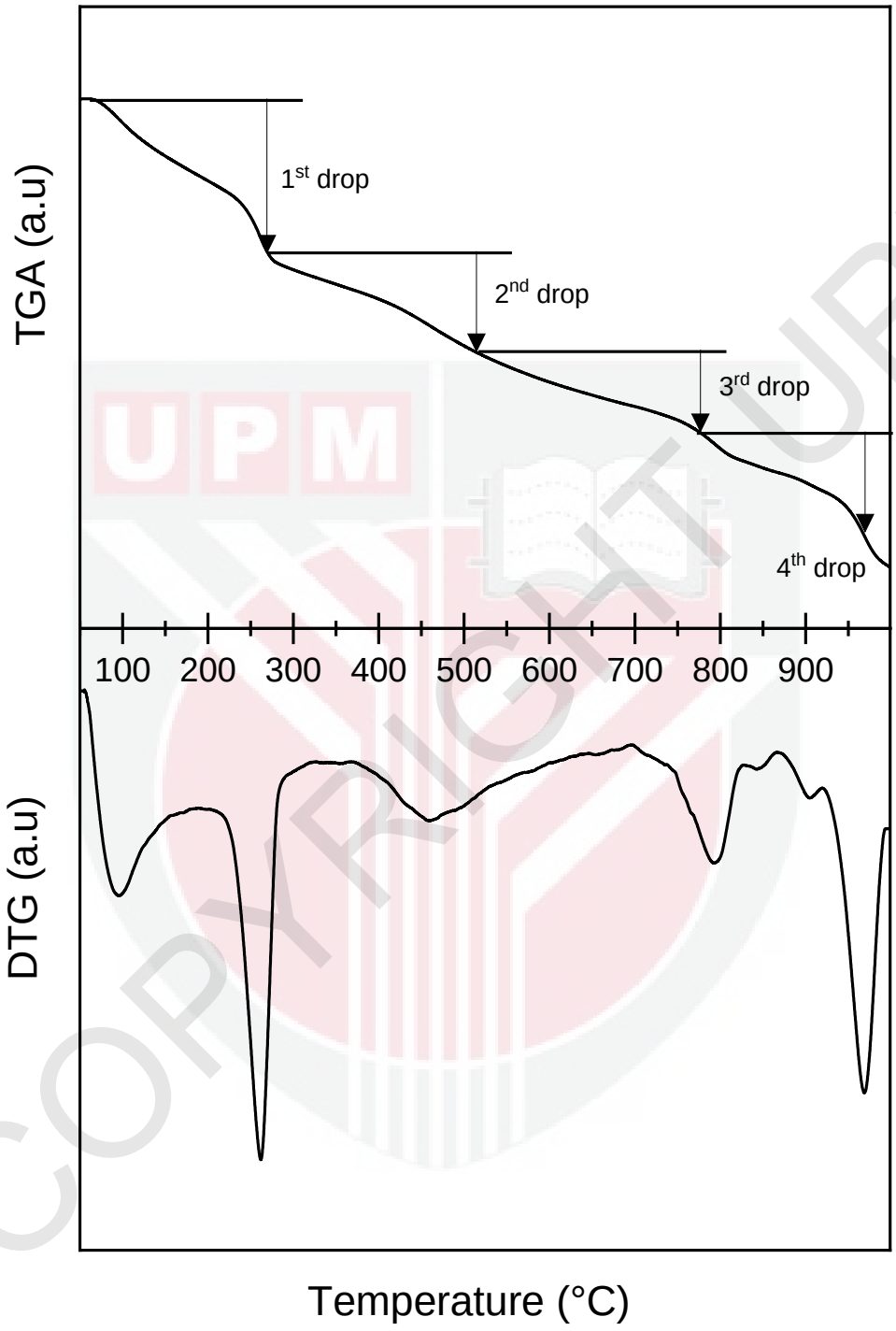

Figure 4.1: TGA and DTG thermograph for pure Y-123 prior sintering.

4.3 X-ray Diffraction (XRD)

4.3.1 The influence of sintering temperatures on phase formation and crystallite size in XRD analysis.

The X-ray Diffraction was utilised to identify superconducting phases, crystal structure, lattice parameters, crystallite size and residual strain of the samples. The samples were measured at 20°-80° (2 Theta) and the X-ray patterns data was analyzed by X'Pert Highscore Plus software which included the Rietveld refinement and the ICSD database (Kamarudin et al., 2022) with the Goodness Of Fit (GOF) range from 3 to 5% as show in Table 4.1.

Figure 4.2 depicts the XRD patterns of pure Y-123 when sintering temperatures were different at 920 ℃, 950 ℃ and 980 ℃. All the samples were sintered for 24 hours. Calcination temperature of 910 °C acts as temperature control. The XRD peaks discovered in the samples were Y-123, Y-211, and $BaCuO_2$, with Y-123 (ICSD No. 98-006-0398) representing as the primary phase and $BaCuO_2$ (ICSD No. 98-002-5029) as the secondary phase. The primary phase of Y-123 showed that the highest intensity are recorded at approximately $2\theta = 32.84°$ with Miller indices (103) implying that all samples were invariably in the orthorhombic phase. Based on the peak pattern in Figure 4.2, the orthorhombic structure (Pmmm) space group of the Y-123 is prominent to all samples with the presence of two secondary peaks, which this peak pattern reason was same to the past research (Khalid et al., 2020).

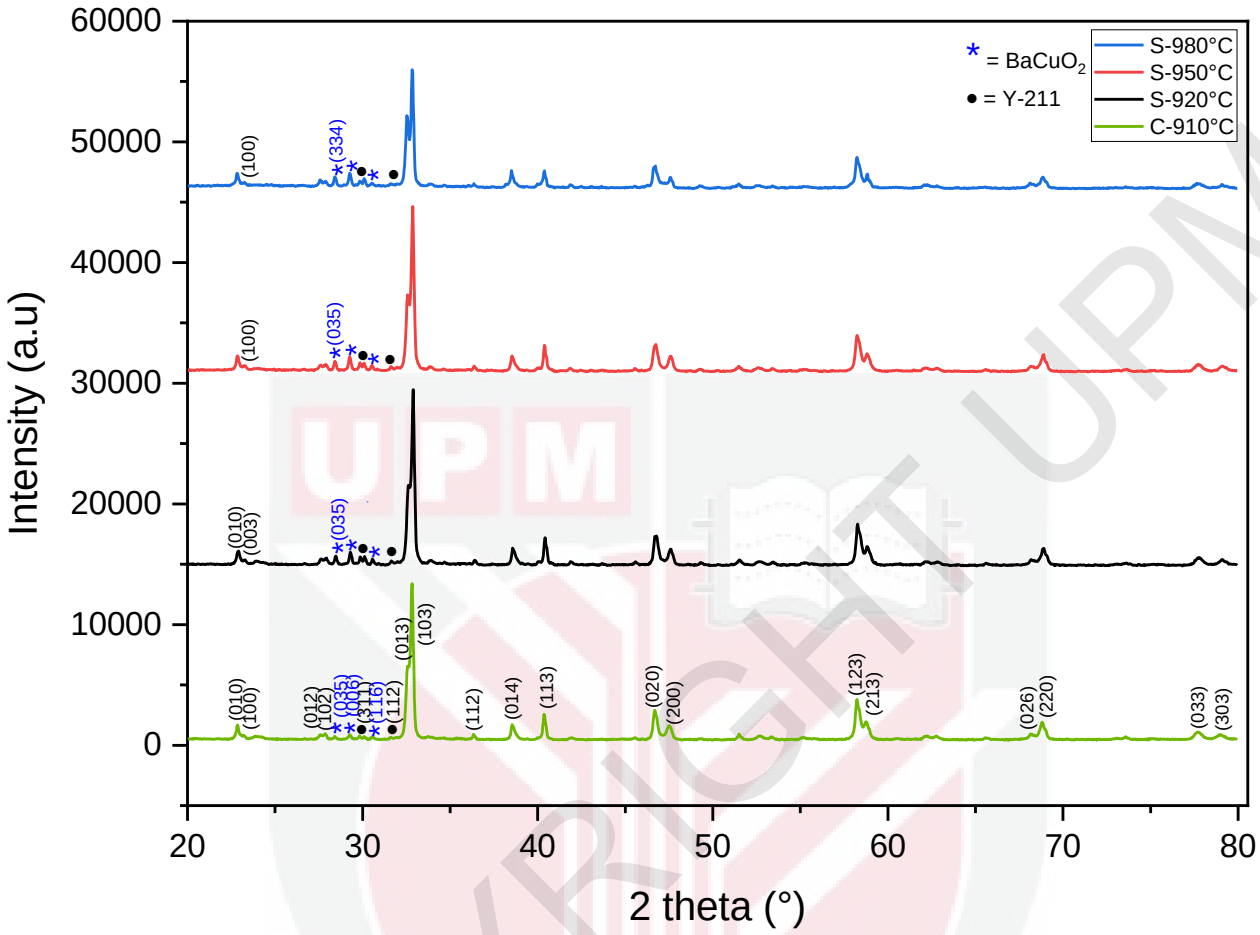

Figure 4.2 : The X-ray Diffraction pattern of sample Y-123 with different temperatures 920 ℃, 950 ℃ and 980 ℃. The calcination temperature of 910 ℃ helps as temperature control.

Table 4.1: The GOF value was determined for different sintering temperatures. The calcination temperature of 910 °C helps as a temperature control.

Sample	GOF (%)
C-910 ℃	5.360
S-920 ℃	4.881
S-950 ℃	3.513
S-980 ℃	5.665

Table 4.2: The lattice parameter, Unit Cell Volume and Orthorhombicity at different sintering temperatures. The calcination temperature of 910 °C helps as a temperature control.

Sample	Lattice parameter			Unit Cell Volume (Å^3)	Orthorhombicity [(*a*-*b*)/(*a*+*b*)]
	***a*(Å)**	***b*(Å)**	***c*(Å)**		
C-910 ℃	3.8272 ± 0.0002	3.8842 ± 0.0003	11.6688 ± 0.0012	173.4626	0.0074
S-920 ℃	3.8247 ± 0.0002	3.8856 ± 0.0003	11.6763 ± 0.0010	173.4330	0.0079
S-950 ℃	3.8224 ± 0.0002	3.8830 ± 0.0002	11.6807 ± 0.0008	173.3709	0.0079
S-980 ℃	3.8198 ± 0.0003	3.8823 ± 0.0003	11.6775 ± 0.0012	173.1679	0.0081

Table 4.1 shows the lattice parameter, unit cell volume and orthorhombicity of the samples was determined. At 910 ℃, the sample was undergone calcination process and the lattice parameter of this sample showed a = 3.8272 Å, b = 3.8842 Å, and c = 11.6688 Å. The lattice constant a decreased during the sintering temperature is 920 ℃, while the lattice constants b and c raised by 0.001 Å to 3.88555 Å and 0.007 Å to 11.67639 Å, respectively. Then, at sintering temperature 950 ℃, the lattice constant a and b were decreased by 0.002 Å to 3.82239 Å and 3.88303 Å. However, the lattice constant c is continually to rise by 0.004 Å to 11.68074 Å. Lastly, all the lattice constant were subsequently fell when the sintering temperature is 980 ℃, the decreases value of lattice constant a, b and c were 0.002 Å to 3.81973 Å, 0.001 Å to 3.88226 Å, and 0.003 Å to 11.67749 Å. Conclusively, the temperature significantly impacts lattice parameters since it aids in the formation of YBCO crystal.

Besides, Table 4.2 also indicate Y-123 phase's orthorhombicity which was derived by using the $(a-b)/(a+b)$ formula where the b and a were the lattice constant (Mousa Dihom et al., 2017). The increase in orthorhombic structure is influenced by lattice parameters (Kamarudin et al., 2022). The amount of oxidation of Y-123 is indicated by its orthorhombicity. Thus, the greater the orthorhombicity, the higher oxygen is contained in Y-123 (Orlova & Laval, 2007). However, an increase in orthorhombicity was observed at 980℃ sintering temperature. This orthorhombicity increased due to the vary dropping of lattice constant a and b. Therefore, the decreasing in orthorhombicity of Y-123 will influenced the T_c, since the copper chain which behaved as a charge reservoir was reduced (Orlova & Laval, 2007).

Table 4.3: The value of Crystallite size and lattice strain of the sample

Sample	Crystallite size Y-123 (µm)	Lattice strain (%)
C-910 ℃	652	0.252
S-920 ℃	637	0.255
S-950 ℃	647	0.253
S-980 ℃	679	0.244

The crystallite size and lattice strain of the samples at different temperature were stated in Table 4.3. Thus, the Scherrer equation can be used to compute the average crystallite size and lattice strain (Mousa Dihom et al., 2017).

$$d = \frac{k\lambda}{\beta \cos \theta} \quad (3)$$

Where k = 0.9

λ is the wavelength of XRD Cuκα radiation source

β is the intensity of highest peak

θ bragg angle

However, the convenient method to determine the crystallite size and lattice strain of Y-123 is by using the Scherrer calculator in the Xpert HighScore Plus software with the highest peak intensity of Y-123 from each sample was chosen. The Miller indices with (103) were picked as the highest peak of Y-123 for each sample to determine their crystallite size and lattice strain. The smallest particle size within a grain was referred to as crystallite size. The greater the crystallite size at a certain plane, the higher X-ray diffraction occurs upon the plane. This will lead to increasing the plane's intensity peak. Moreover, since the grain is formed as a clump of crystallites thus, the grain size could be computed from crystallite size.

From the table 4.3, as the sintering temperature of 920 ℃, 950 ℃, and 980 ℃ was implemented to the sample, the trend revealed from decreased to an increase in crystallite size with 637 µm, 647 µm and 679 µm, respectively. However, the crystallite size for the sample of calcination temperature 910 ℃ showed 652 µm and this sample functioned as a control temperature.

In addition, lattice strain also was discussed in table 4.3 where the term of lattice strain attribute to a lattice that has been distorted or not in its usual state. The peak position of the XRD peak may be shifted due to lattice strain.

4.4 AC Susceptibility (ACS)

4.4.1 The influence of sintering temperatures on T_c and T_p of YBCO by ACS.

According to Dihom et al (2017), Magnetic characterisation is the best method to analyze high temperature superconductor compounds because of their granular in nature (Mousa Dihom et al., 2017). However, the magnetic manifestation of zero resistance is a material which considered to be a superconductor if it exhibits perfect diamagnetic shielding (Meissner effect) with a susceptibility, χ value is at -1 (Ramli, 2015). Thus, AC Susceptibility was utilized to identify the critical temperature, (T_c) which resistivity approaches to zero. The real part of the ACS result was analyzed and normalised between -1 and 0, [-1, 0] where the Y-123 is non-superconducting when the magnetization is 0 and superconducting when the magnetization is -1.

The graph of normalization susceptibility for χ' and χ" against temperature is shown in Figure 4.3. The imaginary part of the curve was between 0 and 1, whereas the real part was between -1 and 0. The real component, χ', indicates the characteristics of intrinsic and coupling diamagnetic shielding, while the imaginary component, χ", reveals the characteristics of coupling losses indicate the common behaviour of sintered ceramic superconductors. From the curve of χ' and χ", the onset diamagnetism, $T_{c\text{-onset}}$ and the coupling peak, T_p were obtained. Next, the phase lock-in temperature, T_{cj}, is the temperature during superconducting grains begin to flow the current (inter-grain) which also can be observed from the graph of ACS . However, from Figure 4.3, T_{cj} cannot be observed for 920 ℃ due to the magnetization out of the measurement range (< 77 K). At sintering temperature 920 ℃, the sample does not showed any critical magnetization trend since superconducting properties have yet to be discovered at this sintering temperature. Meanwhile, at a sintering

temperature of 950 ℃, the magnetization of ACS resulted in a faster drop compared to 980 ℃. From this figure, the three samples showed the magnetization was approaching -1 at the temperature of 78 K.

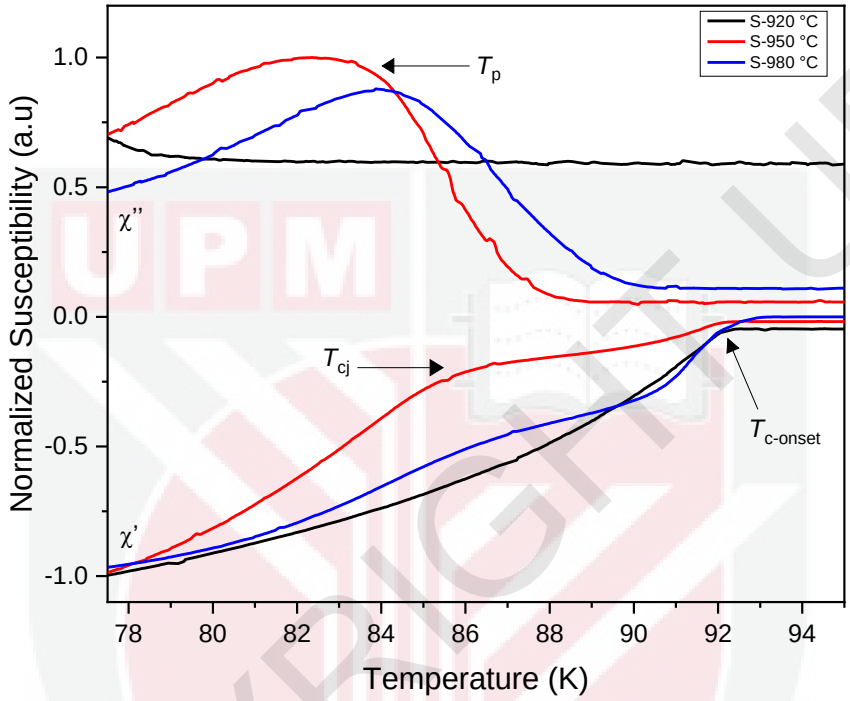

Figure 4.3: The graph of normalization of susceptibility of χ' and χ'' against the temperature.

Table 4.4: The table of $T_{c\text{-}onset}$ and T_p with their corresponding samples.

Sample	$T_{c\text{-}onset}$ (K)	T_{cj}	$T_{c\text{-}onset}$ - T_{cj}	T_p (K)	I_o (μA)
S-920 ℃	92.054	-	-	-	-
S-950 ℃	92.149	86.680	5.469	82.814	24.377
S-980 ℃	93.043	87.219	5.824	84.350	23.337

From the Table 4.4, the $T_{c\text{-onset}}$, T_{cj}, T_p and I_o was determined from the ACS graph. As the sintering temperature is raised, the $T_{c\text{-onset}}$, T_{cj}, and T_p value increase. The sample with a sintering temperature 980 ℃ showed the highest $T_{c\text{-onset}}$, T_{cj}, and T_p value compared to 950 ℃ and 920 ℃. The $T_{c\text{-onset}}$ with the most incredible value indicated that the AC field is strong enough to penetrate the grains. Peak near T_c indicates field penetration into the grains or hysteresis loss caused by intragranular Abrikosov vortices moving within the grains. Besides, according to Sharma et al. (2015), as the separation of the intra and inter-granular dissipation peaks decreases with an increasing sintering temperature, it will reduce grain coupling. Therefore, the grain coupling deterioration will affect the analysis of the field dependence of inter-granular dissipation peak formed at temperature T_p. However, T_{cj} at sintering temperature of 920 ℃ was not visible which showed the wide separation between $T_{c\text{-onset}}$ and T_{cj}, thus, indicating poor coupling within the samples.

The value of Josephson's current, I_o, was also determined in this characterization. Table 4.4 shows the I_o was decreased as the sintering temperature increased. According to the Ambegaokar-Baratoff theory, the value of Josephson's current, I_o, can be obtained from the following equation:

$$I_o = 1.57 \times 10^{-8} \left(\frac{T_{c-onset}{}^2}{T_{c-onset} - T_{cj}}\right) \quad (4)$$

4.5 Scanning Electron Microscopy (SEM)

4.5.1 The influence of sintering temperatures on microstructure in SEM analysis.

In this project, an Scanning Electron Microscopy was carried out to analyze the change in microstructure and surface morphology of Y-123 samples where each of the samples was sintered at a different temperature. All of the sample images were viewed with three difference magnification which are × 3000, × 5000 and × 10,000. These various magnifications were used to acquire a clear image of the grain pattern. Moreover, the average grain sizes were also calculated using Image-J software with 100 grains randomly selected from SEM image as listed in table 4.4. As predicted, the grain size of Y-123 is increased as the temperature of the sample rose and this SEM result coincided with the XRD crystallite size. The technique of measuring average grain size is depicted in Figure 4.4.

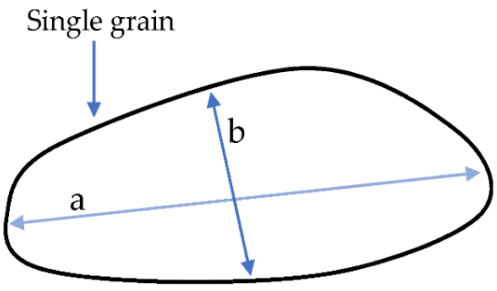

Figure 4.4: The technique of measuring average grain size is illustrated in a schematic diagram (Kamarudin et al., 2021).

The analysis revealed that the pure Y-123 for each sample has an irregular shape and spread randomly and created a strong compacted structure with reduced porosity. Porosity refers to the ratio of pore space in a porous material that is not filled by rock grains in the bulk volume (Fanchi, 2000). Figures 4.5, 4.6 and 4.7 showed the SEM micrograph on surface morphology with different sintering temperatures under different magnification scales which are × 3000, × 5000 and × 10000 respectively. As can be seen in Figure 4.5, the sintering temperature of 920 ℃ showed the grains had an irregular shape with a bunch of porosity on the sample surface compared to 950 ℃ sintering temperature where it illustrates that the observed grain size of this sample has slightly increased and less porosity on the surface. In contrast, the sample that was sintered at 980 ℃ showed the grain size was in irregular surface shapes with larger grains size due to the compactness and homogeneity of this sample were enhanced. Therefore, as the porosity decreases, the connection between the grains might be enhanced (Dihom et al., 2017).

Table 4.5 shows the average grain sizes for each sample. The increasing trend of the samples and average grain sizes commence with sintering temperature of 920 ℃, 950 ℃ and 980 ℃ that has an average grain size of 0.860 μm, 1.149 μm and 1.285 μm respectively. According to the table, the sample with a sintering temperature of 980 °C has the largest average grain size, while the sample with a sintering temperature of 920 °C has the smallest. Therefore, it is fair to conclude that as the temperature increases, the average grain size rises. Hence, as the temperature rises, the grain sizes grow larger, the sample's porosity reduces, the surface morphology enhances and the microstructure becomes more compact which these factors will contribute to enhanced superconducting properties.

Table 4.5: The value of average grain sizes for each sample.

Samples	Average Grain Sizes (μm)
S-920 ℃	0.860 ± 0.414
S-950 ℃	1.149 ± 0.452
S-980 ℃	1.285 ± 0.744

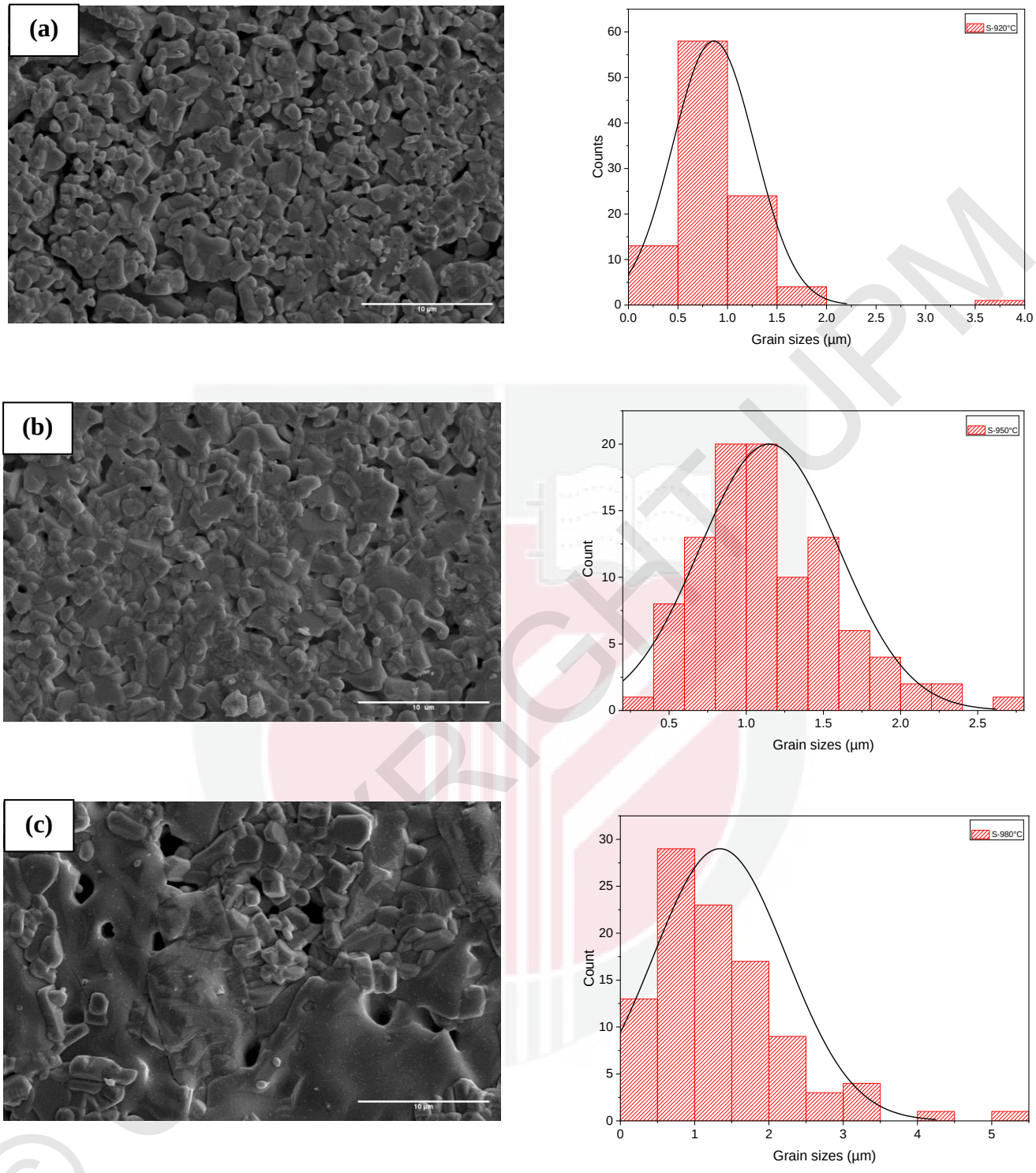

Figure 4.5: SEM micrographs and histogram on surface morphology under magnification × 3000 with different sintering temperature (a) 920 ℃ (b) 950 ℃ and (c) 980 ℃

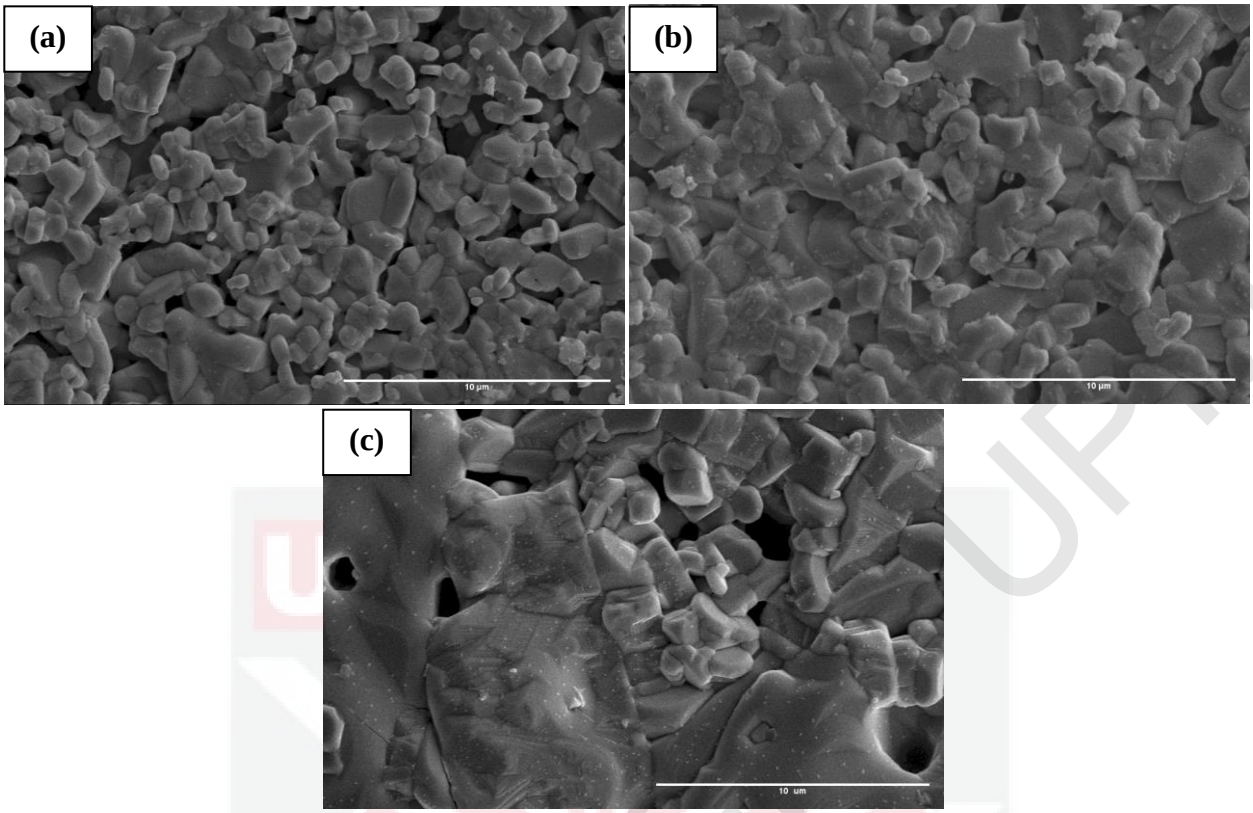

Figure 4.6: SEM micrographs on surface morphology under magnification of × 5000 with sintering temperature (a) 920 ℃ (b) 950 ℃ and (c) 980 ℃

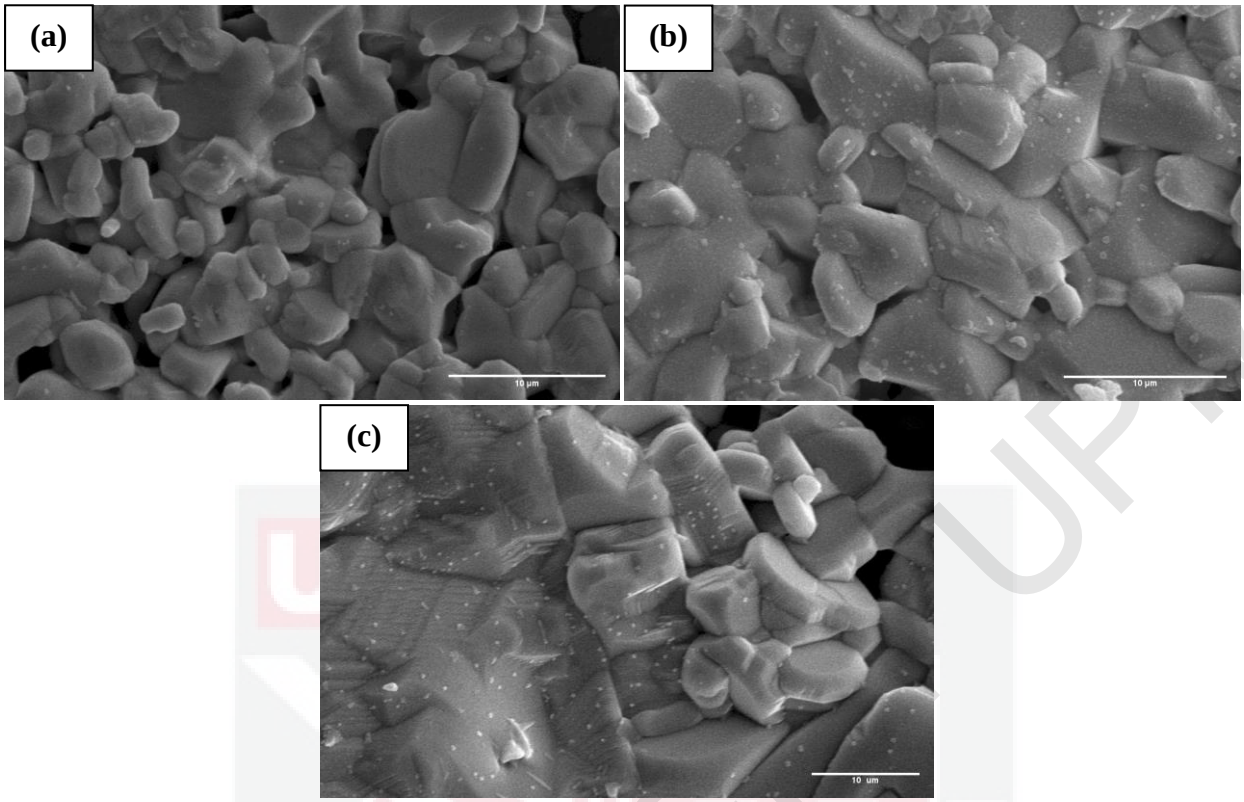

Figure 4.7: SEM micrographs on surface morphology under magnification of × 10,000 with sintering temperature (a) 920 ℃ (b) 950 ℃ and (c) 980 ℃

4.5.2 Energy Dispersive X-ray

The Energy Dipersive X-ray (EDX) tools was used to analyze all of the elements present in the Y-123 superconductor. Thus, In this project, elemental composition in Y-123 was obtained at different sintering temperatures. Table 4.6 shows the atomic percentage of element contained in each sample and the simplest ratio of Y-123 was determined as in table 4.7. Table 4.7 shows the simplest ratio for the sample that is sintered at 920 ℃ with the ratio is 1 : 2.02 : 3.20 while the ratio for sintering temperature 950 ℃ display 1 : 1.75: 2.57 and for the sintering temperature of 980 ℃ reveal the ratio is 1 : 2.15: 3.37. All the sintered sample at temperature of 920 ℃, 950 ℃ and 980 ℃ prove that it satisfies the Y-123 ratio. As the EDX goal is to validate the phase of Y-123 exist in the samples hence, the value of the simplest ratio was approximately close to 1 : 2 : 3. This indicated that the elemental compositions for all the samples were in a pure YBCO ratio.

Table 4.6: The atomic percentage of Y-123 at different sintering temperatures.

Sample	Atomic percentage (%)			
	Y	Ba	Cu	O
S-920 ℃	8.46	17.09	27.09	47.36
S-950 ℃	9.46	16.55	24.33	49.66
S-980 ℃	7.92	16.99	26.71	48.39

Table 4.7: The simplest ratio of the elements with various sintering temperatures.

Sample	Ratio		
	Y	Ba	Cu
S-920 ℃	1.00	2.02	3.20
S-950 ℃	1.00	1.75	2.57
S-980 ℃	1.00	2.15	3.37

4.6 Resistance Measurement from Four Point Probe (4PP)

4.6.1 The influence of sintering temperatures on T_c for Y-123 by 4PP.

Figure 4.8 represents the results of utilizing four point probe (4PP) analysis to determine the transition temperature, T_c. This figure shows the temperature dependence of the electrical resistivity for 920 ℃, 950 ℃ and 980 ℃. From the Figure 4.8, the metallic behaviour of the normal state was revealed to be semiconducting in the sample sintered at 920 ℃. However, when the sintering temperature increased to 950 ℃ and 980 ℃, the YBCO system at the normal state region converted from semiconducting behaviour to superconducting behaviour. This implies that sintering temperatures above 950 ℃ to 980 ℃ promoted superconducting properties and at this temperature range could be the ideal temperature for undergoes sintering process.

On the other hand, the sample for the sintering temperature of 950 ℃ and 980 ℃ were exhibited a two-step transition. This is due to the phase separation in YBCO at various doping levels (Ramli, 2015). According to Mellekh et al (2006), the double transition is an intrinsic property of the YBCO superconductor order parameter (Mellekh et al., 2006). The sintering temperature could also impact coupling strength because as the temperature rises, the coupling strength between the grains decreases. Besides, the occurrence of a double superconducting transition can be related to the another superconducting phase, which could be caused by the different sintering temperature for each sample. The graph of derivative resistance against temperature was also shown in Figure 4.9, in order to provide a clear picture of each samples.

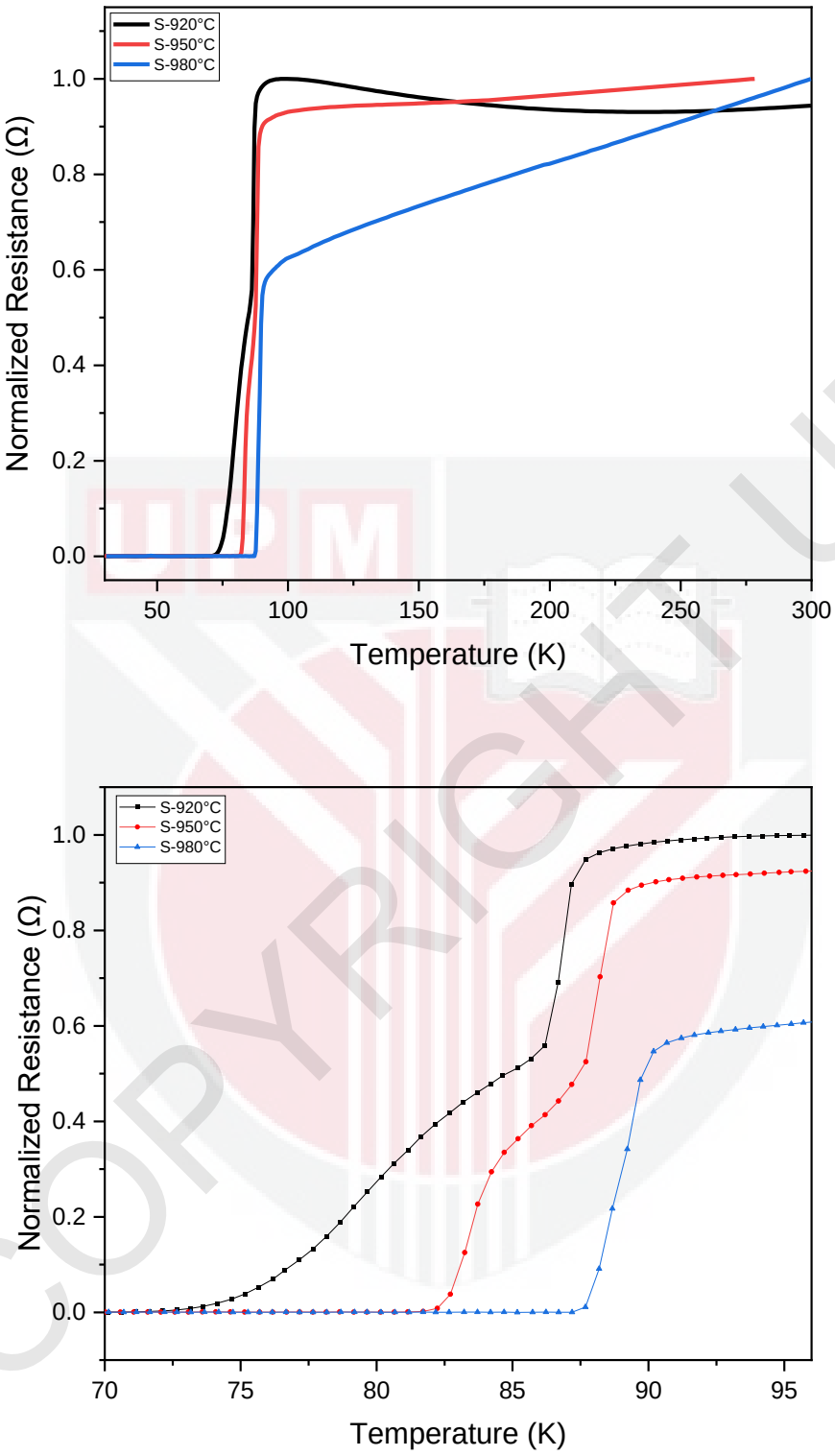

Figure 4.8: The graph of normalized resistance against temperature of Y-123 sintered at different temperatures.

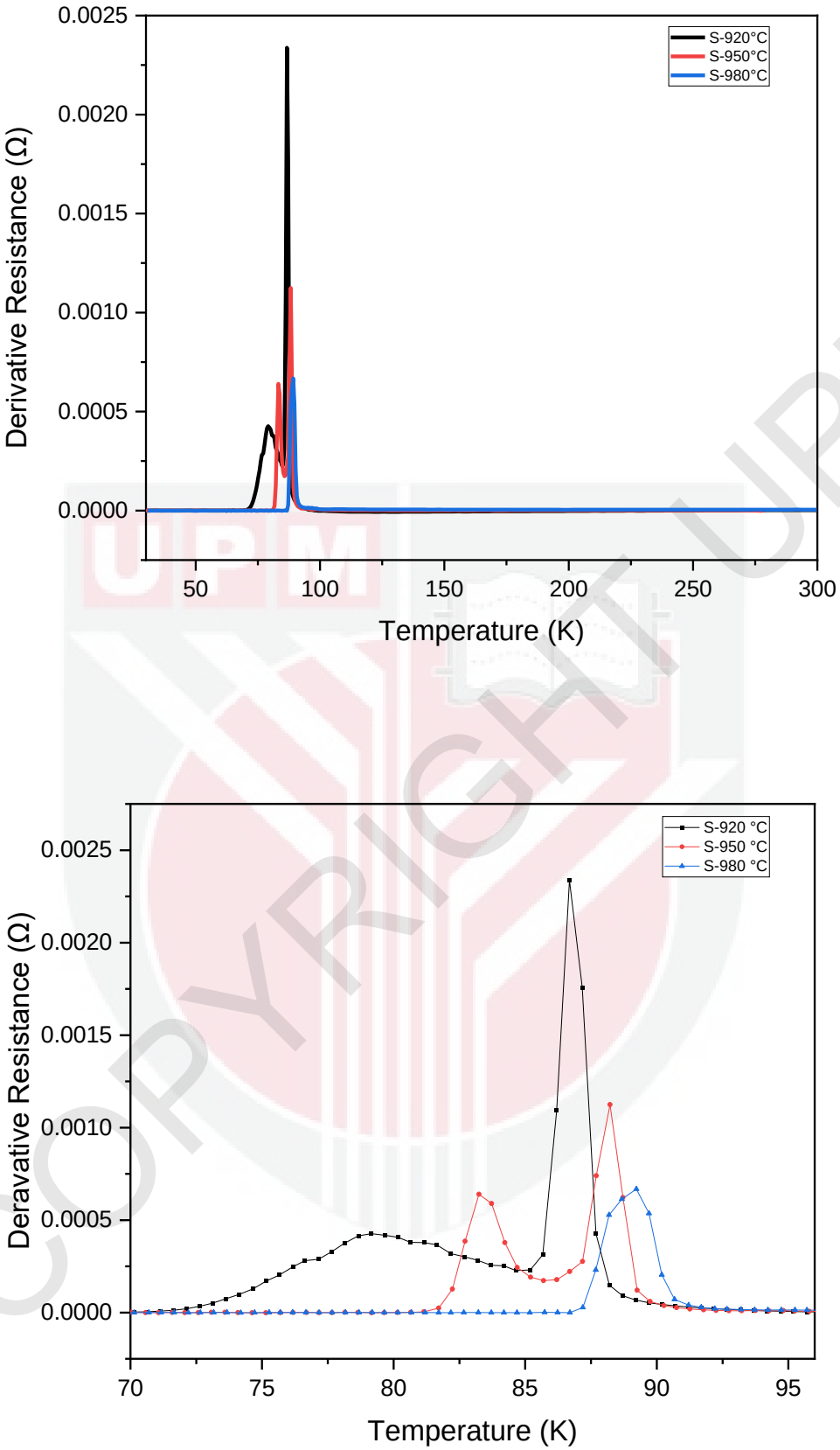

Figure 4.9: The graph of derivative resistance against temperature of Y-123 sintered at different temperatures.

Table 4.8: The $T_{c\text{-onset}}$, $T_{c\text{-offset}}$, and ΔT for Y-123

Samples	$T_{c\text{-onset}}$ (K)	$T_{c\text{-offset}}$ (K)	ΔT (K)	Hole Concentration (p)
S-920℃	88.199	71.657	16.542	0.138
S-950℃	89.744	81.198	8.546	0.143
S-980℃	90.675	86.701	3.974	0.147

The ($T_{c\text{-onset}}$) and zero resistance temperature ($T_{c\text{-offset}}$) values were shown in Table 4.1. Based on the result shown in Table 4.8, the $T_{c\text{-onset}}$ and $T_{c\text{-offset}}$ of sample 920 ℃ is 88.199 K and 71.657 K, for the sample of 950 ℃ is 89.744 K and 81.198 K while for the sample of 980 ℃ is 90.675 K and 86.701 K. All the sample show the $T_{c\text{-onset}}$ is within the range 88 K to 91 K wheras $T_{c\text{-offset}}$ is between 71 K and 87 K. This describes the trends of all the samples for both $T_{c\text{-onset}}$ and $T_{c\text{-offset}}$ increasing as the temperature is raised. Additionally, an increase in T_c could be linked to an increase in oxygen content in the CuO chain, which is created by a reduction in the per CuO_2 plane (Mousa Dihom et al., 2017).

Next, the transition temperature range, ΔT could be seen in the table as well where $\Delta T = T_{c\text{-onset}} - T_{c\text{-offset}}$. In contrast to the samples of 920 °C and 950 °C, the sample of 980 °C had the lowest ΔT. The minor difference in superconducting critical temperature between the samples can be attributed to differences in size and morphology. A smaller particle size results in a slight decrease in T_c (Alikhanzadeh-Arani et al., 2013). Therefore, the lowest value of ΔT might be due to the sample has the best superconducting properties. Besides, the data of hole concentration, p for each sample is also included in table 4.1. The lowest value of hole concentration is 0.138 at 920 °C sintering temperature, opposed to 0.143 at 950 °C

sintering temperature and 0.147 at 980 ℃ sintering temperature. It has been observed that the sintering temperature of 980 ℃ has the lowest T_c with the highest hole concentration as compared to other samples. Thus, when the oxygen content induced into the YBCO system increased, the hole concentration at the CuO_2 plane increased, contributing to the decreasing in ΔT value (Mousa Dihom et al., 2017). As a result, the system's superconducting properties will improve.

Chapter 5

CONCLUSION AND SUGGESTION

5.1 Conclusion

In this project, the sample of Y-123 was synthesized by thermal treatment method with different sintering temperatures without the flow of oxygen where five characteristics were undergone. Hence, the characterization's results from TGA/DTG, XRD, ACS, SEM and 4PP were obtained in order to clarify the project's objective and problem statement.

According to the TGA/DTG results, the sintering temperature for Y-123 was between 867 to 989 °C. Therefore, TGA and DTG measurements could be used to predict the temperature range for pre-calcination, calcination, and sintering process.

The samples were analyzed based on XRD characterization to determine superconducting phases, crystal structure, lattice parameters, crystallite size, and residual strain. From the XRD results, each samples of different sintering temperatures showed Y-

123 as the primary phase while Y-211, and BaCuO2 act as the secondary phase where the primary phase of Y-123 indicates that all samples with Miller indices (103) were in the orthorhombic phase. Besides, the temperature also impacts lattice parameters since it promotes the formation of YBCO crystals. The increasing orthorhombicity and crystallite size was observed at 980°C sintering temperature due to the vary dropping of lattice constant a and b. However, at 980 ℃ sintering temperature, the lattice strain showed the lowest value from the other samples and this might be due to the peak position of the XRD peak shifted.

The ACS results indicated that the sample with a sintering temperature of 920 °C could not be observed attributed to magnetization beyond the measuring range (<77 K), since superconducting properties have yet to be detected at this sintering temperature. Next, $T_{c\text{-onset}}$, T_{cj}, and T_p also was obtained from ACS. Therefore, in comparison to 950 °C and 920 °C, the sample with a sintering temperature of 980 °C had the greatest $T_{c\text{-onset}}$, T_{cj}, and T_p value. The highest $T_{c\text{-onset}}$ value indicated that the AC field is powerful enough to permeate the grains. The value of Josephson's current, I_o, was also determined and it showed as sintering temperature increased, the I_o value decreased.

The SEM characterization was performed to determine the change in microstructure, surface morphology and average grain size of the sample. In this project, all the samples showed an irregular shape but with a different trend of porosity and average grain size. The sintering temperature of 980 °C showed the largest average grain size of approximately 1.285 µm whereas the sintering temperature of 920 °C showed the smallest average grain size of about 0.860 m. Hence, as the sintering temperature rises, less porosity on the surface is observed, and the sample's compactness and homogeneity increase, and so does the average grain size.

Next, an EDX analysis was performed to determine the elemental composition of Y-123. Therefore, in this project, EDX revealed that all samples sintered at temperatures of

920°C, 950°C, and 980°C satisfied the Y-123 ratio, indicating that all samples had pure YBCO ratio elemental compositions.

In order to determine the samples on the transition temperature, T_c, a four point probe was used in this project. Thus, the metallic behaviour of the normal state was found to be in a semiconducting condition in the sample that was sintered at 920 °C. However, when the sintering temperature was increased to 950 °C and 980 °C, the YBCO system in the normal state region converted from semiconducting to superconducting behaviour. As a result, sintering temperatures between 950 °C and 980 °C enhance the superconducting properties. Besides, A two-step transition was observed in the sample for sintering temperatures of 920 °C and 950 °C which is due to phase separation in YBCO at different levels of doping and it might have effect on coupling strength between the grains. Furthermore, all samples reveal that the $T_{c\text{-onset}}$ is between 88 and 91 K, while the $T_{c\text{-offset}}$ is between 71 and 87 K. The trends show that all the sample for both $T_{c\text{-onset}}$ and $T_{c\text{-offset}}$ are increasing as the temperature is raised. Next, as compared to other samples, the sintering temperature of 980 °C has the lowest T_c with the largest hole concentration value which help in improving superconducting properties.

5.2 Recommendation and suggestion

Based on observations of theoretical and experimental results, it is advised that further research should be conducted in the following areas. A few suggestions was listed below:

1. Since this project was not flowing gas, the thermal treatment method should be conducted with flowing gas for upcoming project. As a result, the differences between flowing gas and non-flowing gas can be compared and observed.
2. To investigate the superconducting properties in a specific material, Y-123 can be replaced with Y-358.
3. Different synthesis methods could be employed to determine the superconducting material in the future.

VITAE

Name	:	Nur Afiqah binti Mohamed Indera Alim Sah
Matric Number	:	197955
Programme	:	Bachelor of Science in Physics with Education (Honours)
Session	:	2019/2022
Address	:	No, 67 Kampung Bukit Iboi, 09200 Kupang, Kedah.
Phone Number	:	013-8242398
Email	:	afiqahindera@gmail.com
Background Study	:	

- S.K Syed Sheh
- S.M.K Baling
- Kolej Matrikulasi Kedah
- Universiti Putra Malaysia

REFERENCES

Aarnink, R., & Overweg, J. (2012). Magnetic resonance imaging: A success story for superconductivity. *Europhysics News*, *43*(4), 26–29. https://doi.org/10.1051/epn/2012404

Ali, A. B. (2015). *Effects Of MgO, MgB_2 and Ybco Addition on Formation, Microstructure and Superconducting Properties of $Bi_{1.6}Pb_{0.4}Sr_2Ca_2Cu_3O_4$ Ceramic*. http://psasir.upm.edu.my/id/eprint/65430/1/FS 2015 37IR.pdf

Alikhanzadeh-Arani, S., Salavati-Niasari, M., & Almasi-Kashi, M. (2013). Influence of the utilized precursors on the morphology and properties of $YBa_2Cu_3O_{7-y}$ superconducting nanostructures. *Physica C: Superconductivity and Its Applications*, *488*, 30–34. https://doi.org/10.1016/j.physc.2013.02.007

Ba[a]anda, M. (2013). Study of Condensed Matter by Neutron Scattering and Complementary Methods AC Susceptibility Studies of Phase Transitions and Magnetic Relaxation: Conventional, Molecular and Low-Dimensional Magnets. *Acta Physica Polonica A*, *124*, 964–975. https://doi.org/10.12693/APhysPolA.124.964

Babaev, E., & Speight, M. (2005). Semi-Meissner state and neither type-I nor type-II superconductivity in multicomponent superconductors. *Physical Review B - Condensed Matter and Materials Physics*, *72*(18), 1–5. https://doi.org/10.1103/PhysRevB.72.180502

Bardeen, J. (1955). Theory of the Meissner effect in superconductors [12]. *Physical Review*, *97*(6), 1724–1725. https://doi.org/10.1103/PhysRev.97.1724

Bharat, A. (2018). Superconductors and its Applications 1. *International Journal of Pure and Applied Mathematics*, *119*(12), 7377–7386.

Dagotto, E. (1994). Correlated electrons in high-temperature superconductors. *Reviews of Modern Physics*, *66*(3), 765–841.

https://doi.org/https://doi.org/10.1103/RevModPhys.66.763

Divekar, P. S., & Ekbote, T. (2019). Design and Analysis of Maglev Trains. *International Journal of Science and Research*, *8*(7), 1444–1449. https://www.ijsr.net/archive/v8i7/ART20199779.pdf

Drobac, D. (1996). Critical exponents from high-precision ac susceptibility data. *Journal of Magnetism and Magnetic Materials*, *159*(1–2), 159–165. https://doi.org/10.1016/0304-8853(95)00650-8

Ekinci, A., Uçarkuş, T. Y., Okur, A., Öztürk, M., & Doğan, S. (2017). MRI of pneumonia in immunocompromised patients: Comparison with CT. *Diagnostic and Interventional Radiology*, *23*(1), 22–28. https://doi.org/10.5152/dir.2016.16055

Emily Nagle. (2019). Scanning electron microscopy (SEM) How SEM works. In *Libre Text* (pp. 1–2). https://chem.libretexts.org/@go/page/148465

Fanchi, J. R. (2000). Chapter 3 Porosity. *Developments in Petroleum Science*, *49*(C), 27–40. https://doi.org/10.1016/S0376-7361(00)80028-X

Fields, B. K. K., Demirjian, N. L., Dadgar, H., & Gholamrezanezhad, A. (2021). Imaging of COVID-19: CT, MRI, and PET. In *Seminars in Nuclear Medicine* (Vol. 51, Issue 4, pp. 312–320). W.B. Saunders. https://doi.org/10.1053/j.semnuclmed.2020.11.003

Gopalakrishnan, I. K., Yakhmi, J. V., & Iyer, R. M. (1987). Zero electrical resistance at 106 K in YBa2Cu3O 7-x. *Nature*, *327*(6123), 604–605. https://doi.org/10.1038/327604a0

Kamarudin, A. N., Awang Kechik, M. M., Abdullah, S. N., Baqiah, H., Chen, S. K., Abdul Karim, M. K., Ramli, A., Lim, K. P., Shaari, A. H., & Miryala, M. (2022). Effect of Graphene Nanoparticles Addition on Superconductivity of YBa2Cu3O7~ δ Synthesized via the Thermal Treatment Method. *Coatings*, *12*(1), 91. https://doi.org/10.3390/coatings12010091

Kamarudin, A. N., Kechik, M. M. A., Miryala, M., Pinmangkorn, S., Murakami, M., Chen, S.

K., Baqiah, H., Ramli, A., Lim, K. P., & Shaari, A. H. (2021). Microstructural, phase formation, and superconducting properties of bulk YBa_2Cu_3O superconductors grown by infiltration growth process utilizing the $YBa_2Cu_3O_y$ + $ErBa_2Cu_3O_y$ + $Ba_3Cu_5O_8$ as a liquid source. *Coatings*, *11*(4). https://doi.org/10.3390/coatings11040377

Kaygusuz, K. (2012). Energy for sustainable development: A case of developing countries. *Renewable and Sustainable Energy Reviews*, *16*(2), 1116–1126. https://doi.org/10.1016/j.rser.2011.11.013

Khachan, J., & Bosi, S. (n.d.). *Superconductivity*. Retrieved June 2, 2021, from http://www.physics.usyd.edu.au/~khachan/PTF/Superconductivity.pdf

Khalid, N. A., Awang Kechik, M. M., Baharuddin, N. A., Kien, C. S., Baqiah, H., Pah, L. K., Shaari, A. H., Talib, Z. A., Hashim, A., Murakami, M., & Miryala, M. (2020). Carbon nanofibers addition on transport and superconducting properties of bulk $YBa_2Cu_3O_{7-\delta}$ material prepared via co-precipitation. *Journal of Materials Science: Materials in Electronics*, *31*(19), 16983–16990. https://doi.org/10.1007/s10854-020-04255-0

Khanna, V. K. (2017). Superconductive electronics for ultra-cool environments. In *Extreme-Temperature and Harsh-Environment Electronics Physics, technology and applications*. IOP Publishing. https://doi.org/10.1088/978-0-7503-1155-7ch12

Khare, T., Oak, U., Shriram, V., Verma, S. K., & Kumar, V. (2019). Biologically synthesized nanomaterials and their antimicrobial potentials. In *Comprehensive Analytical Chemistry* (1st ed., Vol. 87). Elsevier B.V. https://doi.org/10.1016/bs.coac.2019.09.002

Khoshnevisan, B., Ross, D. K., Broom, D. P., & Babaeipour, M. (2002). Observations of twinning in $YBa_2Cu_3O_{6+x}$, $0 < x < 1$, at high temperatures. *Journal of Physics Condensed Matter*, *14*(41), 9763–9778. https://doi.org/10.1088/0953-8984/14/41/331

Lee, H. W., Kim, K. C., & Lee, J. (2006). Review of Maglev train technologies. *IEEE Transactions on Magnetics*, *42*(7), 1917–1925.

https://doi.org/10.1109/TMAG.2006.875842

Lee, P. J., Saion, E., Al-Hada, N. M., & Soltani, N. (2015). A simple up-scalable thermal treatment method for synthesis of ZnO nanoparticles. *Metals*, *5*(4), 2383–2392. https://doi.org/10.3390/met5042383

Luis F. Garcia-Herrera & Henry Price. (2020). Thermogravimetric analysis (TGA) How TGA works. In *Libre Text* (pp. 1–2). https://chem.libretexts.org/@go/page/214241

Maric, M. (1991). Preparation of YBCO and BSCCO high Tc superconductors by solution methods. *Key Engineering Materials*, *53–55*, 647–652. https://doi.org/10.4028/www.scientific.net/kem.53-55.647

Martien, D. (n.d.). Introduction to AC Susceptibility. *LOT-Oriel Group Europe*, 1–4.

McQuarrie, D. A. (2013). *Howard University General Chemistry: Atoms First Approach* (Vol. 53, Issue 9).

Mellekh, A., Zouaoui, M., Ben Azzouz, F., Annabi, M., & Ben Salem, M. (2006). Nano-Al2O3 particle addition effects on $YBa_2Cu_3O_y$ superconducting properties. *Solid State Communications*, *140*(6), 318–323. https://doi.org/10.1016/j.ssc.2006.08.008

Mousa Dihom, M., Halim Shaari, A., Baqiah, H., Mohammed Al-Hada, N., Abidin Talib, Z., Soo Kien, C., Syahidah Azis, R., Kechik, M. M. A., Kean Pah, L., & Abd-Shukor, R. (2017). Structural and superconducting properties of $Y(Ba_{1-x}K_x)_2Cu_3O_{7-\delta}$ ceramics. *Ceramics International*, *43*(14), 11339–11344. https://doi.org/10.1016/j.ceramint.2017.05.339

Orlova, T. S., & Laval, J. Y. (2007). Microstructure and superconducting properties of the DyBaCuO ceramic doped with Na_2CO_3, NaCl, and $KClO_3$. *Physics of the Solid State*, *49*(11), 2058–2064. https://doi.org/10.1134/S1063783407110078

Owens, F. J., & Poole, C. P. (1992). The New Superconductors. In *Chemical and Engineering News* (Vol. 70, Issue 51). https://doi.org/10.1021/cen-v070n051.p024

Prabhakar, B., & Wani, T. A. (2020). Crystal structure visualization and powder diffraction pattern of YBCO superconductor. *AIP Conference Proceedings*, *2281*(October), 1–7. https://doi.org/10.1063/5.0026282

Ramli, A. (2015). *Structural and electrical properties of YBCO added with $ND_2O_3Gd_2O_3$ and Sm_2O_3 nanoparticles*. [Doctoral dissertation, Universiti Putra Malaysia]

Roque, A., Sousa, D. M., Fernão Pires, V., & Margato, E. (2017). Superconductivity and their Applications. *Renewable Energy and Power Quality Journal (RE&PQJ)*, *1*, 322–327. https://doi.org/10.24084/repqj15.308

Sarfraz, A., Raza, A. H., Mirzaeian, M., Abbas, Q., & Raza, R. (2020). Electrode Materials for Fuel Cells. *Reference Module in Materials Science and Materials Engineering*, 1–16. https://doi.org/10.1016/b978-0-12-803581-8.11742-4

Saxena, A. K. (2009). Crystal Structure of High Temperature. *Springer Series in Materials Science*, *125*, 41–57. https://scholar.dgist.ac.kr/bitstream/20.500.11750/1389/1/000001916041.pdf

Sharma, D., Kumar, R., & Awana, V. P. S. (2015). Effect of sintering temperature on the nature of weak links and flux pinning mechanism in $La_{1.85}Sr_{0.15}CuO_4$ superconductor. *IOP Conference Series: Materials Science and Engineering*, *73*(1). https://doi.org/10.1088/1757-899X/73/1/012030

Soyeon Shin. (2015). *Vortex pinning force in superconducting Na-intercalated $Ca_{10}Na_x(Pt_3As_8)(Fe_2As_2)_5$ single crystal*. https://scholar.dgist.ac.kr/bitstream/20.500.11750/1389/1/000001916041.pdf

Tadic, T., & Fallone, B. G. (2012). Design and optimization of superconducting mri magnet systems with magnetic materials. *IEEE Transactions on Applied Superconductivity*, *22*(2), 3–9. https://doi.org/10.1109/TASC.2012.2183871

Van Delft, D., & Kes, P. (2010). The discovery of superconductivity. *Physics Today*, *63*(9),

38–43. https://doi.org/10.1063/1.3490499

Vasilev, Y. A., Sergunova, K. A., Bazhin, A. V., Masri, A. G., Vasileva, Y. N., Semenov, D. S., Kudryavtsev, N. D., Panina, O. Y., Khoruzhaya, A. N., Zinchenko, V. V., Akhmad, E. S., Petraikin, A. V., Vladzymyrskyy, A. V., Midaev, A. V., & Morozov, S. P. (2021). Chest MRI of patients with COVID-19. *Magnetic Resonance Imaging*, *79*(March), 13–19. https://doi.org/10.1016/j.mri.2021.03.005

Vishwakarma, V., & Uthaman, S. (2020). Environmental impact of sustainable green concrete. In *Smart Nanoconcretes and Cement-Based Materials: Properties, Modelling and Applications*. Elsevier Inc. https://doi.org/10.1016/B978-0-12-817854-6.00009-X

Waremra, R. S., & Betaubun, P. (2018). *Analysis of Electrical Properties Using the four point Probe Method*. https://doi.org/10.1051/e3sconf/201873

Wesche, R. (2015). Type II Superconductors. In *Physical Properties of High-Temperature Superconductors* (pp. 69–86). https://doi.org/10.1002/9781118696644.ch4

Wolf, V. Z. K. and S. A. (1992). *Fundamentals Of Superconductivity*. https://doi.org/https://doi.org/10.1007/978-1-4899-2507-7

Zhou, T. (2019). Mechanism of High Temperature Superconductivity : The BCS theory and A New Electron Pairing Medium. https://doi.org/10.13140/RG.2.2.19571.27680

APPENDICES

Name and formula

Reference code:	98-002-0922
Compound name:	Yttrium Dibarium Tricuprate (1/2/3/6.94)
Chemical name:	Yttrium Dibarium Tricuprate (1/2/3/6.94)
Common name:	Yttrium Dibarium Tricuprate (1/2/3/6.94)
ICSD name:	Yttrium Dibarium Tricuprate (1/2/3/6.94)
Chemical formula:	$Ba_2Cu_3O_{6.94}Y_1$
Second chemical formula:	$YBa_2Cu_3O_{6.94}$

Crystallographic parameters

Crystal system:	Orthorhombic
Space group:	P m m m
Space group number:	47
a (Å):	3.8180
b (Å):	3.8890
c (Å):	11.6680
Alpha (°):	90.0000
Beta (°):	90.0000
Gamma (°):	90.0000
Calculated density (g/cm^3):	6.37
Volume of cell (10^6 pm^3):	173.25
Z:	1.00
RIR:	7.61

Subfiles and quality

Subfiles:	ICSD Pattern Inorganic
Quality:	Calculated (C)

Comments

ICSD collection code:	64641
Creation Date:	1/1/1970
Modification Date:	1/1/1970
Calculated Pattern Original Remarks:	Total SOF on at least one site differs from unity (SOF < 0.997 resp. SOF > 1.003)
Structures:	YBa2Cu3O6+x(orh)
Original ICSD space group:	PMMM
ICSD Collection Code:	64641
Original ICSD space group:	PMMM

Deviation of the charge sum from zero tolerable

X-ray diffraction from single crystal

Structure type: YBa2Cu3O6+x(orh)

Rietveld profile refinement applied

The structure has been assigned a PDF number (calculated powder diffraction data): 01-079-0048

Total SOF on at least one site differs from unity (SOF < 0.997 resp. SOF > 1.003)

Structure type: YBa2Cu3O6+x(orh)

Recording date: 6/19/1989

Modification date: 5/24/1990

ANX formula: AB2C3X7

Z: 1

Calculated density: 6.37

R value: 0.063

Pearson code: oP13

Wyckoff code: t s r q2 h e a

Publ. title: Crystal structures of Y Ba2 Cu3-s As O9-g (A = Ni, Zn and Co)

References

Primary reference: Hirabayashi, M. Syono, Y. Kikuchi, M. Kusaba, K. Kajitani, T., *Japanese Journal of Applied Physics, Part 2*, **27**, 354, (1988)

Peak list

No.	h	k	l	d [A]	2Theta[deg]	I [%]
1	0	0	1	11.66800	7.571	2.0
2	0	0	2	5.83400	15.175	2.0
3	0	0	3	3.88933	22.846	9.5
4	1	0	0	3.81800	23.279	3.0
5	0	1	1	3.68946	24.102	0.3
6	1	0	1	3.62867	24.512	0.1
7	0	1	2	3.23593	27.542	2.8
8	1	0	2	3.19468	27.905	5.3

9	0	0	4	2.91700	30.624	0.3
10	0	1	3	2.75006	32.533	48.8
11	1	1	0	2.72449	32.847	100.0
12	1	1	1	2.65312	33.756	0.9
13	1	1	2	2.46857	36.365	2.2
14	0	1	4	2.33353	38.550	9.6
15	1	0	4	2.31792	38.820	2.5
16	1	1	3	2.23146	40.388	13.5
17	0	1	5	2.00100	45.282	0.3
18	1	1	4	1.99109	45.520	0.8
19	0	0	6	1.94467	46.670	22.6
20	0	2	1	1.91805	47.357	0.1
21	2	0	0	1.90900	47.596	14.3
22	2	0	1	1.88395	48.268	0.1
23	0	2	2	1.84473	49.362	0.2
24	2	0	2	1.81434	50.246	0.1
25	1	1	5	1.77234	51.523	3.2
26	0	1	6	1.73933	52.574	1.6
27	1	0	6	1.73284	52.787	1.3
28	1	2	1	1.71393	53.415	1.8
29	2	0	3	1.71370	53.423	1.7
30	2	1	1	1.69548	54.043	0.0
31	0	0	7	1.66686	55.049	1.2
32	1	2	2	1.66101	55.259	1.1
33	2	1	2	1.64421	55.873	0.7
34	0	2	4	1.61796	56.861	0.0
35	2	0	4	1.59734	57.663	0.0
36	1	1	6	1.58282	58.243	31.8
37	2	1	3	1.56820	58.839	15.7
38	0	1	7	1.53206	60.369	0.4
39	1	0	7	1.52762	60.563	0.6
40	0	2	5	1.49386	62.081	2.2
41	1	2	4	1.48972	62.273	1.1
42	2	0	5	1.47758	62.842	3.4
43	0	0	8	1.45850	63.760	0.1
44	1	1	7	1.42186	65.606	1.7
45	1	2	5	1.39116	67.244	0.1
46	2	1	5	1.38125	67.792	0.1
47	0	2	6	1.37503	68.140	4.3
48	0	1	8	1.36562	68.675	1.5
49	1	0	8	1.36247	68.856	12.9
50	2	0	6	1.36230	68.866	13.1
51	2	2	1	1.35305	69.403	0.1
52	2	2	2	1.32656	70.996	0.1
53	0	0	9	1.29644	72.906	0.4
54	0	3	0	1.29633	72.913	0.4
55	1	2	6	1.29369	73.087	0.5
56	0	3	1	1.28841	73.435	0.0
57	1	1	8	1.28584	73.605	1.3
58	2	1	6	1.28570	73.615	1.3
59	3	0	0	1.27267	74.496	0.1
60	0	2	7	1.26553	74.988	1.0
61	3	0	1	1.26516	75.013	0.8
62	2	0	7	1.25558	75.686	0.8
63	3	0	2	1.24342	76.559	0.2
64	2	2	4	1.23428	77.230	0.0
65	0	1	9	1.22990	77.557	4.1
66	0	3	3	1.22982	77.563	4.1
67	1	0	9	1.22760	77.729	4.2
68	1	3	0	1.22751	77.736	4.3

69	1	3	1	1.22077	78.247	0.0
70	3	1	0	1.20955	79.115	5.9
71	3	1	1	1.20310	79.623	0.0
72	1	3	2	1.20121	79.773	0.6
73	2	1	7	1.19485	80.284	0.3
74	0	3	4	1.18462	81.121	0.4
75	3	1	2	1.18436	81.142	0.3
76	2	2	5	1.17646	81.803	1.5
77	1	1	9	1.17066	82.295	1.3
78	1	3	3	1.17059	82.302	1.4
79	0	2	8	1.16676	82.631	0.5
80	3	0	4	1.16648	82.655	0.4
81	2	0	8	1.15896	83.311	0.1
82	3	1	3	1.15498	83.662	1.0
83	0	3	5	1.13322	85.647	0.0
84	1	3	4	1.13141	85.817	0.1
85	0	1	10	1.11758	87.142	1.1
86	3	0	5	1.11731	87.169	1.0
87	1	0	10	1.11586	87.311	6.0
88	2	2	6	1.11573	87.324	5.8
89	2	1	8	1.11069	87.821	1.3

Structure

No.	Name	Elem.	X	Y	Z	Biso	sof	Wyck.
1	O1	O	0.50000	0.00000	0.37630	0.4200	1.0000	2s
2	O2	O	0.00000	0.50000	0.38010	0.4200	1.0000	2r
3	O3	O	0.00000	0.00000	0.15840	1.5800	1.0000	2q
4	O4	O	0.00000	0.50000	0.00000	2.7200	0.9400	1e
5	CU1	Cu	0.00000	0.00000	0.35600	0.5200	1.0000	2q
6	CU2	Cu	0.00000	0.00000	0.00000	0.5200	1.0000	1a
7	Y1	Y	0.50000	0.50000	0.50000	0.4500	1.0000	1h
8	BA1	Ba	0.50000	0.50000	0.18580	1.4200	1.0000	2t

Stick Pattern

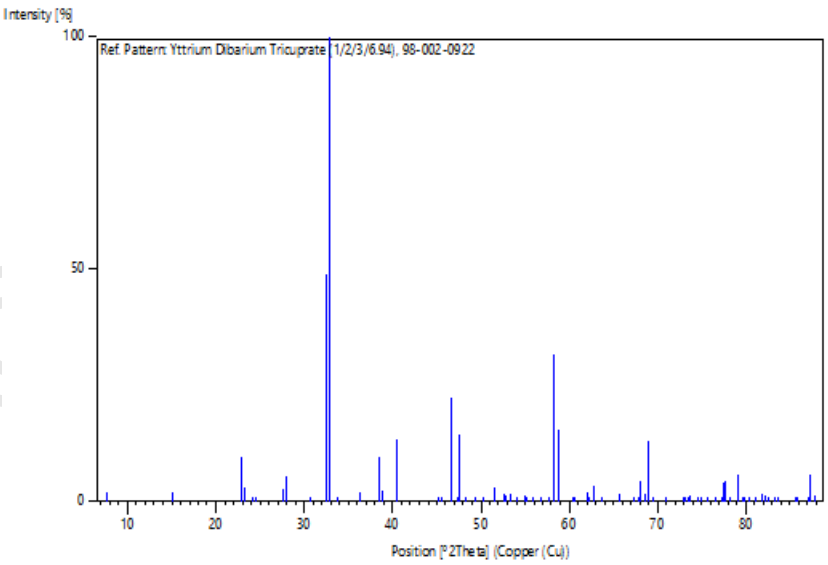

Name and formula

Reference code:	98-003-6464
Compound name:	Yttrium Barium Copper Oxide (1/2/3/6.95)
Chemical name:	Yttrium Barium Copper Oxide (1/2/3/6.95)
Common name:	Yttrium Barium Copper Oxide (1/2/3/6.95)
ICSD name:	Yttrium Barium Copper Oxide (1/2/3/6.95)
Chemical formula:	$Ba_2Cu_3O_{6.95}Y_1$
Second chemical formula:	$YBa_2Cu_3O_{6.95}$

Crystallographic parameters

Crystal system:	Orthorhombic
Space group:	P m m m
Space group number:	47
a (Å):	3.8190
b (Å):	3.8910
c (Å):	11.6730
Alpha (°):	90.0000
Beta (°):	90.0000
Gamma (°):	90.0000
Calculated density (g/cm^3):	6.37
Volume of cell (10^6 pm^3):	173.46
Z:	1.00
RIR:	8.03

Subfiles and quality

Subfiles:	ICSD Pattern Inorganic
Quality:	Calculated (C)

Comments

ICSD collection code:	80733
Creation Date:	1/1/1970
Modification Date:	1/1/1970
Calculated Pattern Original Remarks:	Total SOF on at least one site differs from unity (SOF < 0.997 resp. SOF > 1.003)
Structures:	YBa2Cu3O6+x(orh)
Original ICSD space group:	PMMM
ICSD Collection Code:	80733
Original ICSD space group:	PMMM
	At least one temperature factor missing in the paper

Structure type: YBa2Cu3O6+x(orh)

Rietveld profile refinement applied

The structure has been assigned a PDF number (calculated powder diffraction data): 01-086-0053

Neutron diffraction (powder)

Total SOF on at least one site differs from unity (SOF < 0.997 resp. SOF > 1.003)

Structure type: YBa2Cu3O6+x(orh)

Recording date: 5/13/1997

ANX formula: AB2C3X7

Z: 1

Calculated density: 6.37

R value: 0.065

Pearson code: oP13

Wyckoff code: t s r q2 h e b a

Publ. title: Atomic and magnetic structure of Y Ba2 (Cu1-x (57)Fex)3

O6+y studied by neutron diffraction on isotope enriched samples

References

Primary reference: Mirebeau, I. Lyubutin, I.S. Bouree, F. Balagurov, A.M., *Physica C (Amsterdam)*, **228**, 299, (1994)

Peak list

No.	h	k	l	d [A]	2Theta[deg]	I [%]
1	0	0	1	11.67300	7.567	1.5
2	0	0	2	5.83650	15.168	1.6
3	0	0	3	3.89100	22.837	8.7
4	1	0	0	3.81900	23.273	3.8
5	0	1	1	3.69133	24.090	0.1
6	1	0	1	3.62968	24.505	0.1
7	0	1	2	3.23751	27.529	3.7
8	1	0	2	3.19568	27.896	3.5
9	0	0	4	2.91825	30.610	0.5
10	0	1	3	2.75135	32.517	48.2

11	1	0	3	2.72554	32.834	100.0
12	1	1	1	2.65415	33.743	1.0
13	1	1	2	2.46954	36.350	2.3
14	0	0	5	2.33460	38.531	8.8
15	1	0	4	2.31877	38.805	2.5
16	1	1	3	2.23235	40.371	13.9
17	0	1	5	2.00190	45.261	0.2
18	1	0	5	1.99189	45.501	0.6
19	0	2	0	1.94550	46.649	23.2
20	0	2	1	1.91903	47.332	0.0
21	2	0	0	1.90950	47.582	14.3
22	2	0	1	1.88445	48.255	0.0
23	0	2	2	1.84566	49.336	0.2
24	2	0	2	1.81484	50.231	0.2
25	1	1	5	1.77307	51.500	3.2
26	0	1	6	1.74011	52.549	1.9
27	1	0	6	1.73352	52.764	1.9
28	1	2	1	1.71472	53.388	1.9
29	2	0	3	1.71421	53.406	2.1
30	2	1	1	1.69602	54.025	0.0
31	0	0	7	1.66757	55.023	1.0
32	1	2	2	1.66177	55.232	1.0
33	2	1	2	1.64473	55.854	1.0
34	0	2	4	1.61875	56.831	0.1
35	2	0	4	1.59784	57.644	0.1
36	1	1	6	1.58348	58.216	32.3
37	2	1	3	1.56872	58.818	16.2
38	0	1	7	1.53274	60.340	0.4
39	1	0	7	1.52823	60.536	0.4
40	0	2	5	1.49457	62.048	2.5
41	1	2	4	1.49040	62.241	1.0
42	2	0	5	1.47807	62.819	3.2
43	0	0	8	1.45913	63.730	0.0
44	1	1	7	1.42245	65.576	1.4
45	1	2	5	1.39179	67.209	0.2
46	2	1	5	1.38173	67.765	0.2
47	0	2	6	1.37568	68.104	4.7
48	0	1	8	1.36622	68.640	1.8
49	1	0	8	1.36303	68.824	13.7
50	2	0	6	1.36277	68.839	14.1
51	2	2	1	1.35358	69.373	0.0
52	2	2	2	1.32708	70.964	0.1
53	0	0	9	1.29700	72.870	0.6
54	1	2	6	1.29427	73.049	0.7
55	0	3	1	1.28907	73.391	0.0
56	1	1	8	1.28638	73.570	2.1
57	2	1	6	1.28617	73.584	2.0
58	3	0	0	1.27300	74.473	0.2
59	0	2	7	1.26611	74.947	0.9
60	3	0	1	1.26550	74.990	0.6
61	2	0	7	1.25603	75.654	0.7
62	3	0	2	1.24376	76.535	0.2
63	2	2	4	1.23477	77.194	0.0
64	0	1	9	1.23044	77.516	4.6
65	1	0	9	1.22811	77.691	4.7
66	1	3	1	1.22137	78.202	0.0
67	3	0	3	1.20989	79.088	6.6
68	3	1	1	1.20345	79.595	0.0
69	1	2	7	1.20179	79.727	0.6
70	2	1	7	1.19530	80.248	0.3

71	0	3	4	1.18521	81.072	0.3
72	3	1	2	1.18471	81.114	0.3
73	2	2	5	1.17693	81.763	1.9
74	1	1	9	1.17116	82.253	2.0
75	0	2	8	1.16730	82.584	0.4
76	3	0	4	1.16682	82.626	0.4
77	2	0	8	1.15938	83.273	0.0
78	3	1	3	1.15533	83.631	1.5
79	0	3	5	1.13378	85.595	0.1
80	1	3	4	1.13195	85.766	0.0
81	0	1	10	1.11807	87.095	1.0
82	3	0	5	1.11765	87.136	0.8
83	1	0	10	1.11632	87.266	6.8
84	2	2	6	1.11618	87.280	7.3
85	2	1	8	1.11111	87.779	1.7

Structure

No.	Name	Elem.	X	Y	Z	Biso	sof	Wyck.
1	O1	O	0.50000	0.00000	0.00000	0.5000	0.4750	1b
2	O2	O	0.00000	0.50000	0.00000	0.5000	0.4750	1e
3	O3	O	0.50000	0.00000	0.37900	0.5000	1.0000	2s
4	O4	O	0.00000	0.50000	0.37900	0.5000	1.0000	2r
5	O5	O	0.00000	0.00000	0.15800	0.5000	1.0000	2q
6	CU1	Cu	0.00000	0.00000	0.35600	0.5000	1.0000	2q
7	CU2	Cu	0.00000	0.00000	0.00000	0.5000	1.0000	1a
8	BA1	Ba	0.50000	0.50000	0.18400	0.5000	1.0000	2t
9	Y1	Y	0.50000	0.50000	0.50000	0.5000	1.0000	1h

Stick Pattern

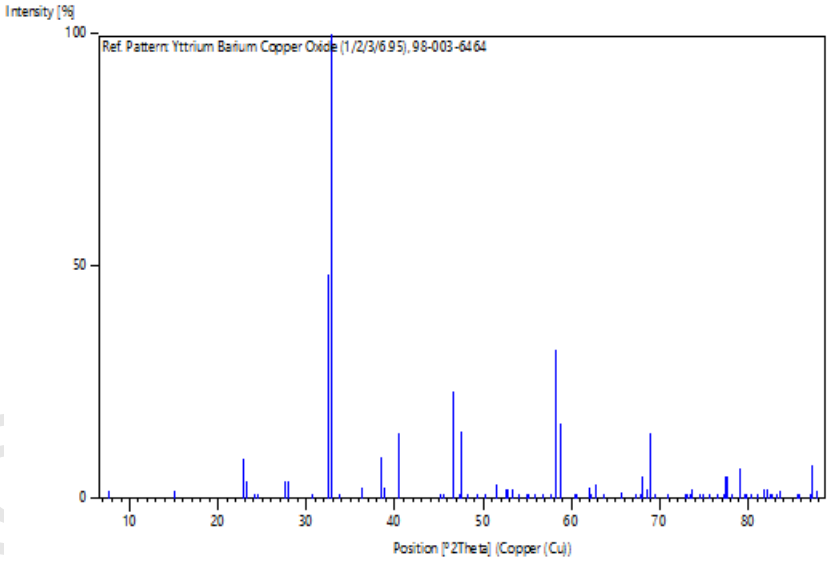

Name and formula

Reference code:	98-002-4855
Compound name:	Yttrium Barium Copper Oxide (1/2/3/6.91)
Chemical name:	Yttrium Barium Copper Oxide (1/2/3/6.91)
Common name:	Yttrium Barium Copper Oxide (1/2/3/6.91)
ICSD name:	Yttrium Barium Copper Oxide (1/2/3/6.91)
Chemical formula:	$Ba_2Cu_3O_{6.91}Y_1$
Second chemical formula:	$YBa_2Cu_3O_{6.91}$

Crystallographic parameters

Crystal system:	Orthorhombic
Space group:	P m m m
Space group number:	47
a (Å):	3.8160
b (Å):	3.8820
c (Å):	11.6740
Alpha (°):	90.0000
Beta (°):	90.0000
Gamma (°):	90.0000
Calculated density (g/cm^3):	6.38
Volume of cell (10^6 pm^3):	172.94
Z:	1.00
RIR:	6.77

Subfiles and quality

Subfiles:	ICSD Pattern Inorganic
Quality:	Calculated (C)

Comments

ICSD collection code:	65590
Creation Date:	1/1/1970
Modification Date:	1/1/1970
Calculated Pattern Original Remarks:	Total SOF on at least one site differs from unity (SOF < 0.997 resp. SOF > 1.003)
Structures:	YBa2Cu3O6+x(orh)
Original ICSD space group:	PMMM
ICSD Collection Code:	65590
Original ICSD space group:	PMMM
	At least one temperature factor is implausible or meaningless but

agrees with the value given in the paper.

Deviation of the charge sum from zero tolerable

Structure type: YBa2Cu3O6+x(orh)

Temperature in Kelvin: 270

Rietveld profile refinement applied

The structure has been assigned a PDF number (calculated powder diffraction data): 01-079-0641

Neutron diffraction (powder)

Total SOF on at least one site differs from unity (SOF < 0.997 resp. SOF > 1.003)

Structure type: YBa2Cu3O6+x(orh)

Recording date: 6/8/1990

ANX formula: ABC2D2X7

Z: 1

Calculated density: 6.38

R value: 0.032

Pearson code: oP13

Wyckoff code: t s r q2 h e a

Publ. title: A study of the Cu-O chains in the high Tc superconductor

Y Ba2 Cu3 O7 by high resolution neutron powder diffraction

References

Primary reference: Fischer, P. Marezio, M. Strobel, P. Capponi, J.J. Hewat, A.W. Yvon, K. Junod, A. Francois, M., *Solid State Communications*, **66**, 1117, (1988)

Peak list

No.	h	k	l	d [A]	2Theta[deg]	I [%]
1	0	0	1	11.67400	7.567	2.0
2	0	0	2	5.83700	15.167	2.3
3	0	0	3	3.89133	22.835	8.0

4	0	1	0	3.88200	22.890	8.5
5	1	0	0	3.81600	23.292	3.7
6	0	1	1	3.68367	24.141	0.4
7	1	0	1	3.62714	24.523	0.1
8	0	1	2	3.23240	27.573	3.2
9	1	0	2	3.19400	27.911	5.9
10	0	0	4	2.91850	30.608	0.4
11	0	1	3	2.74828	32.554	55.2
12	1	0	3	2.72456	32.846	98.7
13	1	1	0	2.72135	32.886	100.0
14	1	1	1	2.65030	33.793	1.2
15	1	1	2	2.46646	36.397	2.9
16	0	0	5	2.33480	38.528	10.0
17	0	1	4	2.33278	38.563	9.0
18	1	0	4	2.31822	38.815	2.4
19	1	1	3	2.23011	40.413	16.4
20	0	1	5	2.00080	45.287	0.5
21	1	0	5	1.99159	45.508	0.6
22	1	1	4	1.99034	45.538	0.7
23	0	0	6	1.94567	46.645	10.8
24	0	2	0	1.94100	46.764	18.2
25	0	2	1	1.91471	47.445	0.0
26	2	0	0	1.90800	47.622	17.4
27	2	0	1	1.88302	48.294	0.0
28	0	2	2	1.84184	49.445	0.2
29	2	0	2	1.81357	50.269	0.2
30	1	1	5	1.77200	51.533	3.8
31	0	1	6	1.73942	52.572	1.4
32	0	2	3	1.73692	52.653	1.5
33	1	0	6	1.73336	52.770	0.9
34	1	2	0	1.73006	52.878	1.1
35	2	0	3	1.71315	53.441	2.3
36	2	1	0	1.71235	53.468	2.4
37	1	2	1	1.71137	53.501	1.5
38	2	1	1	1.69422	54.087	0.1
39	0	0	7	1.66771	55.018	1.2
40	1	2	2	1.65873	55.342	1.4
41	2	1	2	1.64311	55.914	0.9
42	0	2	4	1.61620	56.929	0.1
43	2	0	4	1.59700	57.677	0.1
44	1	1	6	1.58275	58.246	23.8
45	1	2	3	1.58086	58.322	25.8
46	2	1	3	1.56732	58.875	18.6
47	0	1	7	1.53230	60.359	0.4
48	1	0	7	1.52815	60.540	0.6
49	0	2	5	1.49258	62.140	2.9
50	1	2	4	1.48822	62.342	1.1
51	2	0	5	1.47742	62.850	3.8
52	2	1	4	1.47691	62.874	3.6
53	0	0	8	1.45925	63.724	0.0
54	1	1	7	1.42194	65.602	1.8
55	1	2	5	1.39004	67.306	0.2
56	2	1	5	1.38080	67.816	0.3
57	0	2	6	1.37414	68.190	5.4
58	0	1	8	1.36593	68.657	1.9
59	1	0	8	1.36299	68.826	5.7
60	2	0	6	1.36228	68.867	8.4
61	2	2	0	1.36068	68.960	10.2
62	2	2	1	1.35153	69.493	0.0
63	2	2	2	1.32515	71.083	0.2

64	0	0	9	1.29711	72.863	0.3
65	0	3	0	1.29400	73.066	0.5
66	1	2	6	1.29287	73.140	0.8
67	0	3	1	1.28612	73.587	1.1
68	1	1	8	1.28603	73.593	1.2
69	2	1	6	1.28543	73.633	1.6
70	2	2	3	1.28442	73.701	1.4
71	3	0	0	1.27200	74.541	0.2
72	0	2	7	1.26493	75.029	0.9
73	3	0	1	1.26452	75.058	0.8
74	0	3	2	1.26333	75.141	0.3
75	2	0	7	1.25567	75.680	0.9
76	3	0	2	1.24283	76.602	0.3
77	2	2	4	1.23323	77.309	0.0
78	0	1	9	1.23025	77.531	1.5
79	1	0	9	1.22810	77.692	5.1
80	0	3	3	1.22789	77.708	5.4
81	1	3	0	1.22546	77.891	4.3
82	1	3	1	1.21876	78.401	0.1
83	3	0	3	1.20905	79.154	7.4
84	3	1	0	1.20876	79.176	7.4
85	3	1	1	1.20234	79.683	0.1
86	1	2	7	1.20069	79.815	0.6
87	1	3	2	1.19931	79.925	0.2
88	2	1	7	1.19472	80.294	0.4
89	3	1	2	1.18365	81.201	0.3
90	0	3	4	1.18294	81.260	0.4
91	2	2	5	1.17561	81.875	2.1
92	1	1	9	1.17091	82.275	0.5
93	1	3	3	1.16887	82.449	1.8
94	0	0	10	1.16740	82.576	0.3
95	0	2	8	1.16639	82.663	0.3
96	3	0	4	1.16606	82.691	0.3
97	2	0	8	1.15911	83.297	0.0
98	3	1	3	1.15435	83.718	1.6
99	0	3	5	1.13180	85.781	0.1
100	1	3	4	1.12990	85.960	0.1
101	0	1	10	1.11794	87.107	1.3
102	3	0	5	1.11699	87.200	0.8
103	3	1	4	1.11677	87.222	1.0
104	1	0	10	1.11633	87.265	1.9
105	1	2	8	1.11545	87.351	5.9
106	2	2	6	1.11506	87.390	6.6
107	2	1	8	1.11066	87.824	1.9

Structure

No.	Name	Elem.	X	Y	Z	Biso	sof	Wyck.
1	O1	O	0.00000	0.50000	0.00000	0.5000	0.9100	1e
2	O2	O	0.00000	0.50000	0.37780	0.5000	1.0000	2r
3	O3	O	0.50000	0.00000	0.37780	0.5000	1.0000	2s
4	O4	O	0.00000	0.00000	0.15880	0.5000	1.0000	2q
5	CU1	Cu	0.00000	0.00000	0.35520	0.5000	1.0000	2q
6	CU2	Cu	0.00000	0.00000	0.00000	0.5000	1.0000	1a
7	Y1	Y	0.50000	0.50000	0.50000	0.5000	1.0000	1h
8	BA1	Ba	0.50000	0.50000	0.18470	0.5000	1.0000	2t

Stick Pattern

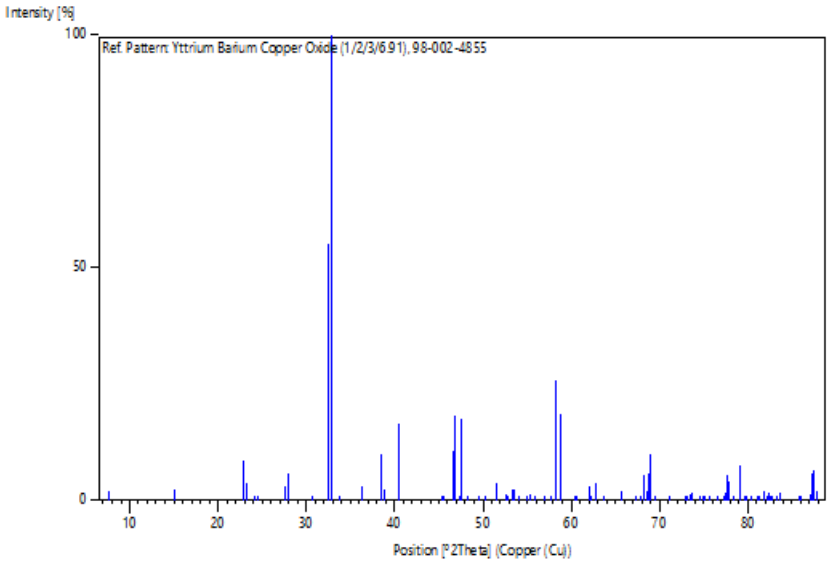

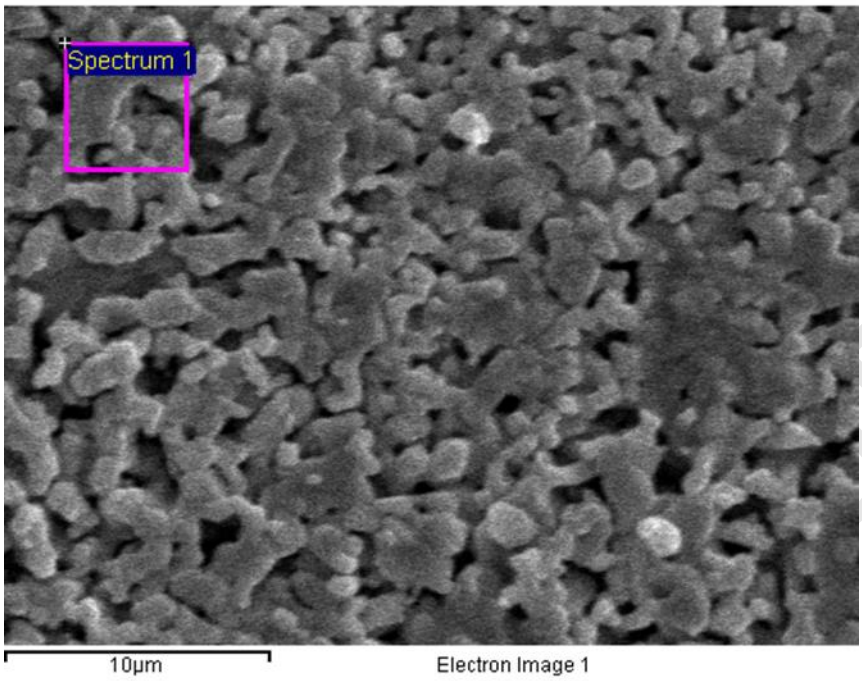

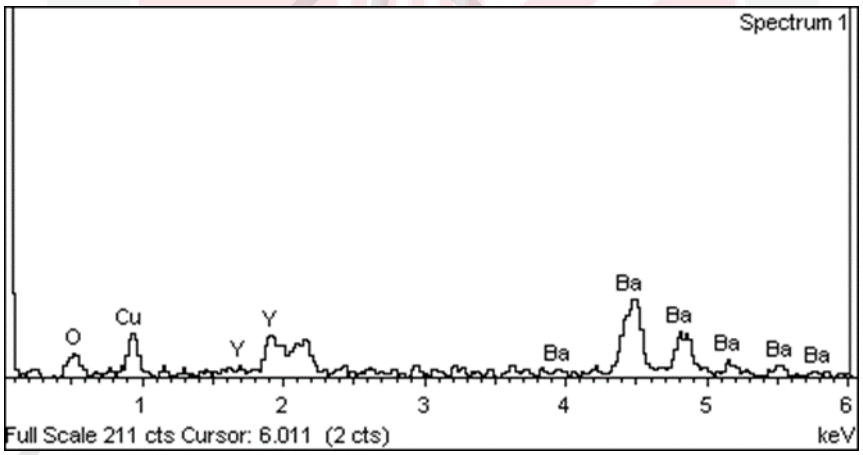

Figure A. 1: The spectrum of sintering temperature 920 °C.

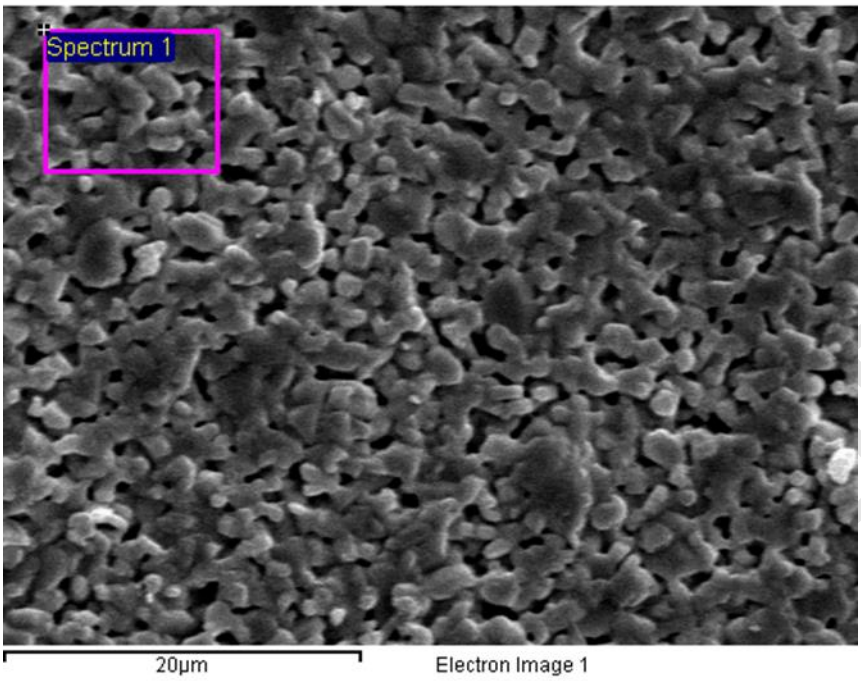

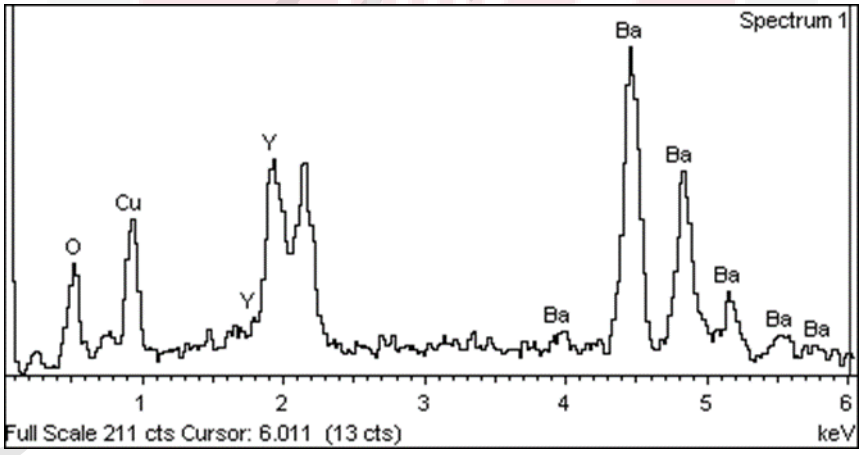

Figure A. 2: The spectrum of sintering temperature 950 °C.

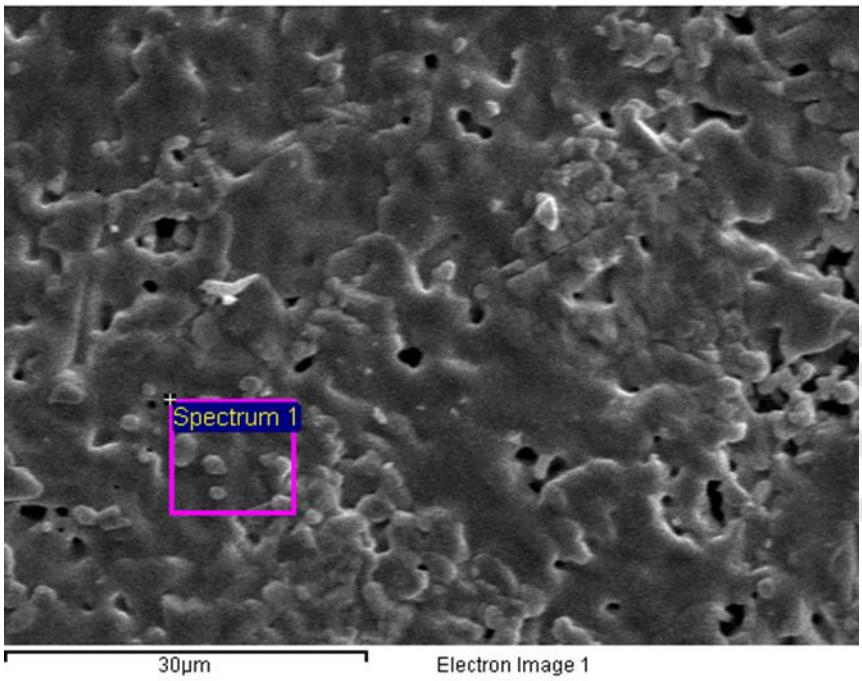

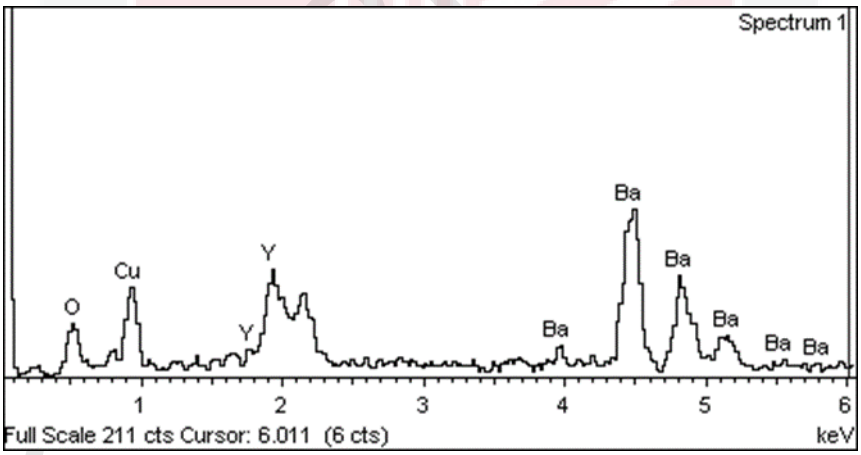

Figure A. 3: The spectrum of sintering temperature 980 °C